THIN FILM BASED SEMI–ACTIVE RF MARKER DESIGN FOR INTERVENTIONAL MRI DEVICES

by

Engin Baysoy

B.S., Electrical and Electronical Engineering, Başkent University, 2006

M.S., Biomedical Engineering of Institute of Science, Başkent University, 2009

Submitted to the Institute of Biomedical Engineering

in partial fulfillment of the requirements

for the degree of

Doctor

of

Philosophy

Boğaziçi University

2018

ACKNOWLEDGMENTS

I would like to express my greatest gratitute to my family for their endless support throughout my thesis study. I would like to thank my mother Gülnur Baysoy, my father Halit Baysoy and my brother Emre Baysoy for always believing in me and being my moral support through my ups and downs.

I would like to thank my supervisor, Assoc. Prof. Dr. Özgür Kocatürk, for his guidance and helping me to learn many different manufacturing methods in biomedical engineering throughout this thesis. He showed me the whole side of the picture.

I am also thankfull to Prof. Dr. Şenol Mutlu for his valuable advices and opening his laboratory for usage of me without any hesitation for many years.

My special words of thanks should also go to my committee members Prof. Dr. Yekta Ülgen and Prof. Dr. Cengizhan Öztürk for their time and scientific advices throughout the progress of this thesis.

It was a real pleasure for me to be a part of Institute of Biomedical Engineering of Bogazici University. I would like to thank to Ayşegül Ünal and Çiğdem Günsür for their help at the administration. I would like to mention Dr. Bora Büyüksaraç who was always a phone call away to help me to finish this thesis study on time.

My special statements of regards go to Prof.Dr.İrfan Güney, Assoc. Prof. Dr. Alpay Özcan, and Assist. Prof. Dr. Emin Aksoy for their encouragement during last year.

This thesis is carried out as a part of the project which is supported by TUBITAK (Scientific and Technical Research Council of Turkey) under contract of 112R024.

ACADEMIC ETHICS AND INTEGRITY STATEMENT

I, Engin Baysoy, hereby certify that I am aware of the Academic Ethics and Integrity Policy issued by the Council of Higher Education (YÖK) and I fully acknowledge all the consequences due to its violation by plagiarism or any other way.

Name :

Signature:

Date:

ABSTRACT

THIN FILM BASED SEMI–ACTIVE RF MARKER DESIGN FOR INTERVENTIONAL MRI DEVICES

Compared to the other imaging modalities Magnetic Resonance Imaging (MRI) system has many advantages. There is a great demand to carry out interventional cardiovascular procedures under MRI scanner. However, the lack of visible markers and MRI compatible interventional instruments and devices, is the main problem for realizing clinical applications with MRI guidance. In order to provide widespread usage of MRI for endovascular operations, commercial catheters and guidewires must be manufactured by considering many performance criteria including visualization, miniaturization, flexibility and safety.

In this thesis, clinical grade biocompatible polymers and metals were used to manufacture clinical grade MRI compatible RF markers. Proposed RF marker was deposited on a non–planar biocompatible catheter surface by physical vapor deposition (PVD) technique using cylindrical laser–cut shadow masks, which kept the overall device profile low. The presented fabrication approach is highly reproducible, and versatile, allowing variation of micro coils, capacitors, and conducting layer designs that are crucial for tuning the specific resonant frequency of a RF marker.

In adddition to aforementioned work, an orientation independent simulation model was developed and validated to obtain a reliable method for evaluating the designed RF marker structures in a MRI environment. Finite Element Method (FEM) simulations were carried out for different RF coil designs to make the computational analysis of their electrical and magnetic characteristics in COMSOL Multiphysics program.

Keywords: Semi–active RF marker, RF coil, RF receiver antenna, thin–film based techniques, RF heating, FEM simulations, congenital heart diseases.

ÖZET

GİRİŞİMSEL RADYOLOJİDE KULLANILAN CİHAZLAR İÇİN İNCE FİLM TABANLI YARI AKTİF RF İŞARETLEYİCİ TASARIMI

Mevcut görüntüleme modaliteleri ile kıyaslandığında Manyetik Rezonans Görüntüleme (MRG) sisteminin sahip olduğu üstünlüklerin herkes tarafından kabul görmesiyle girişimsel kardiyovasküler ameliyatların MRG tarayıcı ile yapılması yönünde bir eğilim doğmuştur. Ancak halen güvenilir ve MRG uyumlu girişimsel aletlerin mevcut olmaması, bu klinik uygulamaların MRG rehberliğiyle yapılabilmesinin önündeki en büyük sorundur. Klinikteki kalp içi uygulamalarında MRG kullanımının yaygınlık kazanabilmesi için rehber tel ve kateterlerin ticari olarak üretiminde görüntülenebilirlik, küçültülebilirlik, esneklik ve güvenlik gibi kriterlerin dikkate alınması gerekmektedir.

Bu tez çalışmasında, biyouyumlu polimer ve metaller kullanılarak, klinikte kullanılabilir, MRG uyumlu radyo frekans (RF) işaretleyiciler üretilmiştir. Hazırlanan RF işaretleyiciler düz olmayan kateter yüzeyler üzerine lazer kesim gölge maskeler kullanılarak fiziksel buhar kaplama yöntemiyle küçük ölçeklerde kaplanmıştır. Sunulan bu üretim yöntemi çok yönlü özelliği sayesinde, RF işaretleyicilerin belli bir frekansta ayarlanabilmesi için oldukça önem taşıyan birçok farklı mikro bobin, kapasitör veya iletim yolu yapımında kullanılabilecektir.

Bu çalışmalara ek olarak, farklı şekilde dizayn edilmiş RF işaretleyici yapılarının üretimini yapmaksızın güvenilir bir şekilde değerlendirebilmek için, konumdan bağımsız bir simülasyon modelinin uygulanabilirliği doğrulanmıştır. Sonlu eleman yöntemi kullanılarak Comsol Multiphysics programı simülasyonları ile, farklı RF bobin tasarımlarının elektriksel ve manyetik karakteristiği matematiksel olarak analiz edilmiştir.
Anahtar Sözcükler: Yarı aktif RF işaretleyici, RF bobin, RF alıcı anten, ince film teknikleri, RF ısınma, SEM simülasyonları, doğuştan gelen kalp rahatsızlıkları.

TABLE OF CONTENTS

LIST OF FIGURES

LIST OF TABLES

LIST OF SYMBOLS

σ	Electrical conductivity
ρ	Tissue density
E	Electric field magnitude
T	Tesla
B	Magnetic field magnitude
γ	Gyromagnetic ratio
C	Capacitance value
L	Inductance value
f_L	Larmor frequency
f	Resonance frequency
μ	Magnetic permeability
N	Number of coil turns
ε	Permittivity
R_1	Inner radius of circular capacitor
R_1	Outer radius of circular capacitor
ρ	Resistivity
ω	Angular frequency
H_+	Right hand circularly magnetic field
V_S	Signal voltage
V_N	RMS noise voltage per one square-root Hertz
Δf	Full width at half maximum
f_0	Peak frequency
S	Siemens
Cr	Chromium
Au	Gold
$PTFE$	Polytetrafloroetilen

LIST OF ABBREVIATIONS

iCMRI	Interventional Cardiovascular Magnetic Resonance Imaging
3D	Three-Dimensional
MRI	Magnetic Resoance Imaging
SNR	Signal to Noise Ratio
SAR	Specific Absorption Rate
Q	Quality Factor
VSD	Ventricular Septal Defect
CT	Computed Tomography
PVR	Pulmoner Vascular Resistance
RF	Resonant Frequency
RC	Resonant Circuit
FEM	Finite Element Method
PIN	Positive-Intrinsic-Negative
MMCX	Micro-Miniataure Connectors
MEMS	Micro Electro Mechanic Systems
XMR	Multimodality Image Guidance
Gd-DTPA	Gadolinium Diethylenetriamine Penta-Acetic Acid
CMR	Cardiovascular Magnetic Resoanace
CAD	Computer Aided Design
PEC	Perfect Electric Conductor
TE	Time To Echo
TR	Repetition time
CP	Cardiac Pacing

1. INTRODUCTION

1.1 Interventional Cardiovascular MRI (iCMRI)

Newborn patients may suffer from different forms of congenital heart diseases, including pulmonic and aortic stenosis (pulmonic or aortic valve has narrower size compared to normal ones) ventricular septal defects, atrial septal defects (a gap in the atrioventricular septum), coarctation (narrowing) of aorta, aortic aneurysm (a bulge in the wall of a blood vessel) and etc. Currently, open cardiac operations, which are the most common procedures for the treatment of pediatric patients with congenital heart lesions, have high mortality and morbidity rates. Long operation time and infection risk, cost of long treatment periods in hospital and patient discomfort are the other well–known shortcomings of an open surgery.

As an alternative to cardiac surgeries, image guided interventions refers to catheter–based imaging and therapeutic procedures consist of flexible guidewires, tubes (catheters), stents, balloons, and implants used for dilation and closure into cardiac chambers and blood vessels with the guidance of a X–ray based modality. Unfortunately this minimally invasive treatment option for patients in all age groups with varied cardiovascular diseases associated with cancer risk due to ionizing radiation. Pediatric patients are more sensitive to the carcinogenic effects of ionizing radiation than adults, and children have a greater cancer risk as the long term chromosomal damage [1, 2]. On the other hand X–ray based imaging modalities including fluoroscopy, computed tomography (CT), and angiography do not provide sufficient image contrast especially for the soft tissues that are necessary for cardiovascular operations. Interventional therapeutic procedures under x ray based modalities do not only suffer from poor soft tissue contrast, but also are not feasible due to the nephrotoxic effects of radiocontrast materials injected to the patient [3]. X-ray exposure during surgery also increases the risk of cancer [4] and cataract [5] of clinical staff and protective lead clothes increase the risk of orthopedic injuries [6] for the personnel occupied in surgery room.

Magnetic Resonance Imaging (MRI) guidance was intended to be a new platform by operators in order to realize catheter–based imaging and therapeutic procedures without usage of x–ray. Beside of ionizing radiation free imaging modality benefits, operators favor MRI to perform complex interventional cardiovascular operations because of its accepted advantages including superior intrinsic soft tissue contrast and multi slice imaging technique [7]. Furthermore, compared to conventional x ray based modalities it is possible to collect reliable and real time physiologic cardiac parameters via MRI such as flow, volume, pressure, diffusion, perfusion, temperature, motion, and etc. [8].

Interventional cardiovascular magnetic resonance imaging (iCMRI) procedures also have capability to perform tissue characterization, cardiac output, systemic and pulmoner blood flow measurements [9], pulmoner vascular resistance (PVR) index [10], assessment of myocardial perfusion-fibrosis in both ischemic and non–ischemic heart disease [11] and following up patients after surgery.

Animal studies showed the feasibility of catheter-based interventional cardiac treatments under MRI such as abdominal aortic aneurysm (a bulge in the wall of a blood vessel) repair [12], stent—graft placement for aorta [13], stenting of aortic coarctation [14], nitinol occluder devices to repair atrial septal defects in swine [15–17], recanalization of chronic peripheral artery total occlusion (blockage of blood vessels) [18], percutaneous intramyocardial injection with a needle tip [19] in porcine models. Additionally, MRI guided interventions including vena cava filter deployment [20–23] and retrieval [23], ablation of cardiac rhythm disorders, visualization of tissue injuries [24], temperature mapping for electrophysiology [25], biopsy needle trials for prostate and breast [8] have recently been reported.

Despite a large number of promising studies, lack of commercially available MRI safe and visible instruments still makes iCMRI unrealistic for the treatment of cardiovascular diseases. Since MRI physical nature has a high magnetic field inside operation room, conventional interventional instruments and devices that consist of conductive materials cannot be utilized with interventional applications under MRI. Beside of MRI

safety concerns with magnetic field effect and RF induced heating problems, medical devices implanted into patient body have to be visible and possible for tracking while operator steering the catheter through the vessels and cardiac chambers of patient.

For semi–active and active catheter designs, in order to highlight the interventional medical devices under MRI, miniature size resonant frequency (RF) markers have to be placed over catheter shaft. Tuning of resonance frequency (RF) marker at Larmor frequency of MRI scanner, is the key for maximum interaction between RF marker and standard coil connected to MRI scanner.

Currently available RF markers in semi–active or active devices contain conventional components such as solenoid coils, non–magnetic capacitors, diodes, wires, and etc. However, all these rigid analog circuit components and the soldering process itself increase overall device profile and affect device mechanical properties (flexibility, endurance, and etc.) unfavorably. Moreover, especially for the pediatric applications, using rigid circuit components over a distal device shaft possesses the risk of injuring and even perforating the vessel surface during catheter orientation within vasculature [26]. Furthermore all the elements of RF markers and transmission lines must be constructed with MRI compatible materials. If it is neccessary to utilize conductive materials and elements for constructing the RF marker, these components have to be manufactured in smaller profile and successfully sealed off within isolation layers. In brief, when designing a MRI compatible catheter for cardiovascular interventions, many aspects have to be taken into account such as safety, performance, material and physical constraints.

The aim of this study is to introduce a novel thin film based manufacturing technique that enables to fabricate a non–planar RF resonant marker on a clinical grade catheter shaft. The RF resonant marker is composed of micron size conductive thin film layers including solenoid coil, cylindrical plate capacitor, conductive paths and insulation layers that are implanted over a 5 Fr guiding catheter shaft without adversely affecting overall cylindrical shape and flexibility while providing that RF-induced heating risk is at minimum level.

In addition, an orientation independent RF simulation model was validated to obtain a reliable method for evaluating the characteristics of the designed RF marker structures used inside the MRI platform. Finite Element Method (FEM) simulations were carried out for developed RF marker prototypes and different RF coil designs to obtain the computational analysis of their electrical and magnetic characteristics in COMSOL Multiphysics program.

Fabricated RF marker prototype design was placed into a birdcage coil in a MRI simulation environment and its magnetic and electrical characteristics were examined in terms of electromagnetic field homogeneity and B_1 field circularity in the volume of interest. Adding to that performance of different RF coil designs were studied when the RF coil was positioned into different orientations with respect to the birdcage coil in virtual MRI platform.

By delineating an approved simulation platform of a MRI environment, various RF marker designs prototypes can be compared. Proposed simulation platform enables a convenient facility to determine various parameters of micro coils that have significant effects on visibility and safety performance of the candidate designs including signal to noise ratio (SNR), Quality (Q) factor, RF induced heating and specific absorption rate (SAR).

1.2 An Overview of Imaging Techniques for iMRI

Visualization of endovascular devices under MRI guidance is a place of interest for many years. While the interventionist navigate vascular structures by using guidewires or catheters, a conspicuous distal tip and a detectable shaft is necessary.

During invasive operations under MRI scanner, MRI safety is another subject to consider. When RF induced heating, caused by coupling of transmitter and receiver, exceeds safety limits deleterious effects on vascular structures may be occurred.

With ongoing advancements in MR imaging techniques, numerous variations of 3 main approaches (passive, active and semi–active) were presented to impart a useful and reliable visualization technique for devices under MRI.

1.2.1 Passive Imaging Technique

Passive device imaging means that the catheter is directly visualized in the acquired image by its own effect on the spins in the close vicinity of the catheter or guidewire. Passive imaging techniques are based on markers with specific contrast agents or materials mounted on catheter distal tip and/or shaft without any external connections to the MRI scanner. Since passive devices are comprised of paramagnetic, ferromagnetic and ferrimagnetic materials that affect adversely T_1 and T_2 relaxation times, it is possible to obtain a positive or negative contrast between endovascular instruments and background anatomy. Accordingly, passive devices do not incorporate metal components and conductive parts, MRI safety concerns and many mechanical problems can be eliminated automatically.

The presence of materials and markers with a magnetic susceptibility that are different from the magnetic susceptibility of background tissue distorts the uniform main magnetic field, B_0. As a result of the difference in magnetic susceptibility with respect to the surrounding anatomy, the paramagnetic markers produce a local magnetic field inhomogeneity. This inhomogeneity results in magnetic field variations within voxels that cause spins to precess at different frequencies with respect to Larmor frequency of MRI scanner [27, 28].

Simplest passive tracking application is to use contrast–enhanced MRI tools mounted on catheters or guidewires filled with some contrast agents such as 19F [29] and hyperpolarized 13C [30]

Positive contrast tracking consists of ring shaped paramagnetic markers such as dysprosium oxide (Dy2O3) [31], iron oxide particles [32] , gadolinium diethylenetri-

amine pentaacetic acid (Gd-DTPA) [33–36] placed within the lumen or on the surface of a catheter shaft that cause T_1 shortening and bright signal spots (positive contrast) relative to adjacent tissue. As shown in 1.2, the plastic multi chamber cylinders can be also used for positioning of both titanium (paramagnetic) and graphite (diamagnetic) pieces over catheter within different layers to develop a positive contrast tracking device [37].

1.2.2 Active Imaging Technique

Active tracking techniques comprise small receiver coils or antennas placed into the catheter or guidewire for receiving and/or transmitting the signal via separate channels to the MRI scanner. The device visualization can be performed independently from MR imaging with accurate coordinates of interventional devices through vasculature.

In contrast to passive techniques, long conductive transmission lines used in active approaches for transporting electrical signals between the catheter and MRI scanner, result in significant heating which is caused by induced current during RF transmission [43]. Active catheterization may also suffer from limited steerability and flexibility in tortuous blood vessels and cardiac chambers due to the rigid and non–flexible mechanical properties of incorporated RF receiver coils and antennas [44].

First construction attempts for active imaging technique were focused on increasing the signal to noise ratio (SNR) for sampling specific regions by developing two-turn elliptical transceiver coil [45]. One of the simplest way of active systems employed by conveying a small amount of DC current in wires through catheter, cause electromagnetic field inhomogeneity and susceptibility artifact similar to passive methods [46].

For the tracking of endovascular catheters loopless designs were presented [47–49] that incorporate tuning, matching and decoupling circuits in order to supply ef-

ficient SNR and reduce RF induced heating over conductive lines. Combination of loopless antenna concept with biopsy needles and puncture apparatus leaded some therapeutic procedures under animal experiments [50–52].

Despite potential outcomes of loopless catheter-based interventions, further modification was needed in rigid instruments for navigating through delicate vessels. In addition to that since the catheter tip has to be sharp enough to enable biopsy and puncture procedures, positioning of a coil or antenna at distal tip becomes more difficult [52].

In order to overcome flexibility problems, a multi lumen deflectable active catheter was offered that incorporates loop receiver coils. Combination of loop receiver coils with a nitinol laser-cut slotted tube and a nitinol spring was established in order to provide kink resistance during deflection and to help maintain the catheter shape during navigation [53].

Kocaturk and his colleagues [54] fabricated a hybrid catheter shaft consist of a copper and nitinol wire-braided polymer hypotube wire lattice and three distal loop coils over a flexible and steerable 7 Fr device. While loop coils supplies 3 focal image markers on the distal end for tip tracking, the loopless antenna with the wire braided polymer tubing provides shaft visibility of the catheter. In order to minimize RF induced heating on conductive paths a positive-intrinsic-negative (PIN) diode was used that shorts out the connector end of the antenna during MR excitation when a positive direct current voltage is supplied by the scanner.

Another design that was established on a 5 Fr intravascular catheter, incorporates twisted-pair RF coils and a special switching circuitry outside the coil [55]. In order to minimize RF induced heating on transmission lines, the coil was assembled in two different modes that the detuning of tip coil can be switch on and off according to MRI signal and that result in additional time consumption in undergoing procedure.

Adding to that for specific procedures like ablation, catheter withdrawal may be needed before MRI imaging during ablation applications that may result in interventionist to lose the catheter's position at the ablation site so that it would need to be directed back precisely for further ablations [56].

Although many promising studies have been introduced for the realization of active catheters at clinical level, together with safety concerns due to RF induced heating on transmission lines [47, 57, 58] flexibility and visualization problems of the catheter tip have not been solved yet.

1.2.3 Semi–Active (Hybrid) Imaging Technique

Semi–active imaging techniques can also be named as hybrid imaging technique since it embodies some of the specific properties and benefits of both passive and active imaging techniques. Semi–active methods benefit wireless resonant circuits (RC) as fiducial RF marker that inductively couples the standard transmitter/receiver coil of MRI scanner without any connection hardware in between.

Excitation of RF signal by transmit coil results in locally induced B_1 field over the RF coil and thus substantially enhancing the excitation angle in the directly adjacent surroundings of the RF marker [59]. For semi–active designs since the RF coil is completely activated by RF coupling, heating hazards caused by long conductive lines will be avoided inherently.

First attempts for implantation of a RF marker started with fabricating single wire winding resonant coils [60–62] were tuned to the Larmor frequency of the scanner and a non–magnetic capacitor together with soldering materials and relatively short conductive lines. In order to minimize RF heating hazards on conductive components, and obtain electrical isolation and also maintain magnetic field homogeneity, RF coil is generally coated with a biocompatible insulation layer.

Kaiser and his colleagues [63] presented aerosol-deposition process that based on printing catalytic nano-ink palladium seeds over catheter surface with subsequent electroless plating. Thereby the aerosol-deposition simplifies manufacturing of a 3D resonant circuit directly on catheter shaft and provides fiducial markers. However adhesion of the deposited layer and repeatability of the entire process needs to be improved.

One of the most recent studies showed a ultra-thin, flexible, and surface-mountable wireless RF marker provided a robust localization [64]. Multilayer laminated structure consisting of a split-ring resonant helical structure with incorporated layered capacitors to achieve resonance. The proposed structure may be accepted feasible for anatomic marking, miniaturization of device and safety. However the coupling between RF resonator and transmitter and so the visualization of the RF marker is directly depends on resonator's orientation with respect to the standard transmitter of the MRI scanner.

In contrast to the other visualization techniques, determination of device position, minimization of risk due to RF induced heating and combination of biocompatible materials during fabrication makes semi–active tracking approach more convenient for MRI guidance. However, in order to provide a completely reliable and robust method for interventional MRI procedures, softening and miniaturization of rigid and bulky components such as capacitors, soldering materials and conductive lines is an obligation. Adding to that, since the enhanced signal coupled between the RF marker and the standard surface RF coil (receiver/transmitter) is depending on the catheter position and orientation with respect to the standard surface coil and Bo field, an alternative coupling strategy has to be proposed.

1.2.4 Micro Coil Designs

Fabrication process of RF coils used in both active and semi–active tracking under MRI guidance should be considered together with regarding factors; B_0 magnetic strength, B_1 orientation, surface material, stiffness and geometrical dimensions of the

instrument. These parameters are directly effective on performance of MRI markers including induced current, tuning, biocompatibility, SNR, and Q (Quality factor), [63, 65].

In the literature micro fabricated coil designs in different shapes (single loop, double loops, meander, Helmholtz, and etc.) benefits from Micro Electro Mechanic Systems (MEMS) by applying one or a combination of photolithography processes such as thermal/e-beam evaporation and sputtering [26, 66–68], electroplating [26, 69–72], printed circuit board (PCB) etching [73, 74], micro-contact printing [69], focused ion milling [67], and microfluidic techniques [68].

Fundamental designs for micro RF markers were applied in various shapes over planar surfaces [68, 75–80].

Since navigation through tortuous and sensitive vessel branches with planar shaped micro coil samples is not practical in clinical level, following studies focused on designing circular shape micro coil designs by using laser ablation technique [81, 82], lithography based techniques [83], maskless lithography based techniques [81, 84, 85]. Although these methods achieved with fabrication of three dimensional shapes, difficulties on controlling laser ablation depth and misalignment problems between photomasks and patterns restrain the utilization of these methods [86].

In order to reduce the stiffness problem of planar micro coil designs, in several studies planar coils were mounted over a flexible foil [62, 64, 70, 87–89] to wrap it over a circular catheter shaft. However there are several drawbacks of these designs such as enduring on high mechanical stress, adhesion problem of microcoil over circular catheters and guidewires [86], maintaining asymmetric device profile and variation of coil inductance with the bending radius of the device [90].

Another recent approach for manufacturing micro coil is printing catalytic nano-ink containing palladium seeds directly over catheter surface by using an aerosol-deposition process with subsequent electroless plating [63]. Because adhesion of de-

posited layer is strongly depends on the surface character and it has low mechanical stability under dynamic fatigue loading, the reliability and repeatability of the entire process needs to be improved in order to establish batch production for clinical grade catheter implementation [26].

1.2.5 Transmission Line Designs and MRI Safety

As it is mentioned earlier, although there are many advantages of combining catheterization applications with MRI scanner, interventional cardiac procedures in routine is unavailable due to MRI safety concerns. Even if it doesn't have a ferromagnetic property the presence of any kind of metal is not safe in the strong magnetic field environment of a MRI scanner. Metallic based instruments have the potential to interact with the activated RF transmitter that result in amplified RF heating at vicinity of the instrument [57].

RF induced heating problem under MRI is characterized by the specific absorption rate (SAR), which is expressed as the power dissipated in a given volume [91]:

$$SAR = \frac{\sigma E^2}{2\rho} \tag{1.1}$$

where σ is the electric conductivity, ρ is the tissue density and E is the magnitude of the electric field. For all metallic components and conductive lines that interact with body under MRI, SAR has to be examined because the electric field is maximum at the adjacent tissue.

When the electrical length of the metal components of an interventional device exceeds the quarter wavelength length in a body, the RF induced heating risk increases. Therefore, it is offered to utilize a conductive cable length less than a quarter wavelength. The dielectric constant of the tissues and the operating frequency determines the wavelength [92]. This limit is approximately 12 cm for a conductive transmission line within body at 1.5 T MRI scanners.

In order to minimize the RF heating hazards, there are many different presented transmission line designs between RF marker and MRI scanner that are used in both active and semi–active tracking strategies. Coaxial chokes or traps into the coaxial cable were offered to reduce RF induced heating [72,93]. However resonance frequency of these circuits may couple with frequency of unwanted currents that may result in local heating on tissue [94]. Dividing the long conductive paths into short off-resonant sections is another concept that is applied by Vernickel and his colleagues [95]. Although, it is possible to avoid local energy dissipation by using transformers at the connection points, the stray capacitance of transformers leads to capacitive coupling between the short conductor parts. Moreover components of the transformers have to be fabricated by using MRI compatible and flexible materials.

Another study proposed a few different transmission pathway designs indicated in Figure 1.14 including leads with chokes; leads incorporate a series of tuned high-impedance RF traps; "billabong" leads with reversed pathways to cancel opposed induced RF electric field; billabong leads that comprise coils in all section of the pathway [96].

Although all mentioned approaches are promising for minimization of RF heating and construction of safe conductive lines, for integrity of these designs with MRI applications, other determining parameters also have to take into account such as excessive device size, re-manufacturability, biocompatibility, and mechanical properties. Adding to that sequence parameters of MRI scanner has an influence to acquiring the possible lowest SAR during clinical procedures.

1.2.6 Multimodality Image Guidance (XMR) with X-Ray Based Modalities and MRI

Since X–ray based modalities provide limited information about soft intracardiac structures and vessels, there is a tendency to benefit MRI imaging that provides superior soft tissue contrast and data related with cardiac functions. Novel research

and surgery suites in several healthcare centers (Acıbadem Healtcare Group Altunizade Hospital, Istanbul- Turkey; Sunnybrook Health Sciences Centre, Toronto-Canada; Children's National Medical Center, NHLBI, Washington DC-USA) were designed to consolidate X–ray based imaging modalities (Fluoroscopy, Computed Tomography, and/or Angiography) and MRI system in order to enhance diagnostic quality of images and improve the success of real time surgical interventions [97]

This multimodality approach has been applied in animal studies such as biopsy of the myocardial free wall [98] and closure of a ventricular septal defect (VSD) [99,100] that result in relatively reduced imaging times and ionizing radiation compared to conventional x ray based techniques. Adding to that, cardiovascular MRI guidance have been already combined with electrophsyiological studies like anatomic stereotactic catheter ablation [101].

In XMR also named as XFM in the literature, while anatomical and physiological information can be collected via MRI, on the other side conventional implantable devices (catheter, guidewire, biopsy needle, occlude and etc.) can be steered and manipulated by interventionist under X ray acquisition [9]. Unfortunately the patient movement may cause misregistration of images obtained from different modalities, during transferring of the patient via a movable tabletop between modalities. Therefore in order to reduce respiratory and patient motion based artifacts, some special markers and software algorithms can be used during registration of images [11, 97, 98]

2. MATERIALS AND METHODS

2.1 Manufacturing of RF Marker Design

2.1.1 Theorical Parameters of RF Marker Design

In order to provide the depiction of RF marker or antenna (for semi–active or active tracking) under MRI, resonance frequency of RC circuit or antenna have to be tuned at the Larmor frequency of the regarding MRI scanner.

$$f_L = \frac{\gamma}{2\pi} B_0 \tag{2.1}$$

where, f_L is the Larmor frequency, B_0 is the amount of magnetic field, and γ is the gyromagnetic ratio for nuclei of hydrogen atoms. For instance, designed be used under 1.5 Tesla, the resonance frequency for a RF marker, RC circuit has to be around 63.8 MHz.

In the literature there are many different coil and capacitor designs suitable to form RF resonant markers. The resonance frequency of a RF resonant marker can be calculated using the following formula;

$$f = \frac{1}{2\pi\sqrt{LC}} \tag{2.2}$$

where L is the inductance (H), C is capacitance (F) and f is resonance frequency (Hz) of the RC circuit. In our design, L is expressed as;

$$L = \frac{\mu \pi r^2 N^2}{h} \tag{2.3}$$

where r is the radius of the coil, μ is the magnetic permeability of the environment, N is the number of turns, and h is the coil length. Variation on the coil dimensions such as ww (wire width), wp (winding pitch), wt (wire thickness) can be resulted in significant alteration at the amount of L of the RC circuit (Eq. 2.2).

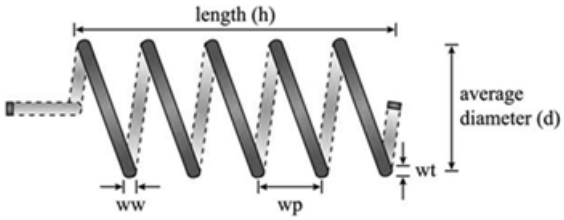

Figure 2.1 Symbolic ilustration of the main parameters for a sample coil.

Capacitance value (C) of a circular capacitor formed on a cylindrical surface is expressed as;

$$C = \frac{2\pi\varepsilon l}{ln(\frac{R_2}{R_1})} \tag{2.4}$$

where ε is the permittivity of the material between capacitor plates ($\varepsilon = \varepsilon_0\ \varepsilon_r$). R_2 is the outer radius, R_1 is the inner radius of capacitor plates, and ε is the permittivity of the material between capacitor plates.

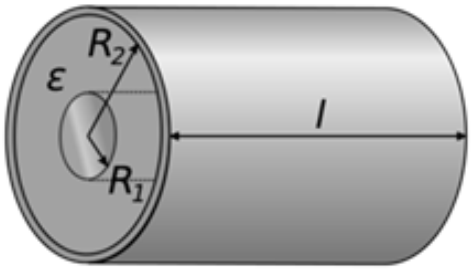

Figure 2.2 Symbolic ilustration of a sample cylindrical capacitor.

An interconnection conductive layer between the coil and the capacitor cause a parasitic capacitance, which has to be considered while calculating the overall capacitance. The contact capacitance of return path (Cc) can be calculated using the general formula of the C,

$$C_c = \varepsilon \frac{A}{d} \tag{2.5}$$

where Cc is the contact capacitance, A is the area of overlap of the two plates, d is the separation length between two plates, and ε is the permittivity of the material between capacitor plates.

In order to reduce the resistivity of the overall conducting paths and overcome the problems of very thin coated surfaces, the conductive layer thickness was optimized by considering the skin depth effect using the following formula;

$$\delta = \sqrt{\frac{2\rho}{\omega\mu}} \tag{2.6}$$

where ρ is the resistivity of the conductor, ω is the angular frequency (2πf), and μ is the magnetic permeability of the conductor.

In order to improve the accuracy of the acquired diagnostic images, performance of the L is very significant in RC circuit. Optimum parameters of the L, can be evaluated in terms of the signal to noise ratio (SNR) and the quality factor (Q). The SNR is the ratio between signal from a small volume of a material in the sample and electrical noise currents generated by thermal power dissipation [102]. It has been reported that the SNR of a receiver coil under MRI depends on both magnetic field strength, and the magnitude of the RF field per unit current [65, 103–106]. Since there are many drawbacks regarding the usage of a high magnetic field (e.g., 3 Tesla) for interventional procedures such as increased complexity of MRI compatibility, additional

RF-induced heating risk, and nerve stimulation from oscillating magnetic fields, there is a tendency to raise the SNR of implanted RF coil under low magnetic fields (e.g., 1.5 Tesla).

The intrinsic SNR is simplified by [47] as below;

$$\psi = \frac{V_S}{V_N}(\frac{H_+}{\sqrt{R}}) \tag{2.7}$$

where V_S is the signal voltage, V_N is the RMS noise voltage per one square-root Hertz, H_+ is the right hand circularly magnetic field component generated by the coil at unit input current, and R is the real part of the input impedance seen from the input terminals of the coil. Since many parameters influence the value of both H_+ and R in order to improve SNR, there is a tradeoff between H+ and R.

In order to evaluate the signal amplification that can be achieved with inductive coupling between RF marker and standard transmitter/receiver coil of MRI scanner the following formula is considered as Quality factor [107];.

$$Q = \omega\frac{L}{R} \tag{2.8}$$

where Q is the quality factor of LC circuit, w_0 is the angular frequency, L is the inductance and R is the impedance of the resonator. The Q factor of a device can also be calculated by plotting the input impedance versus the frequency;

$$Q = \frac{f_0}{\Delta f} \tag{2.9}$$

where f_0 is the peak frequency and Δf is the full width at half maximum.

2.1.2 Outline of fhe Fabication Process of RF Marker Design

In the first part of this thesis, a micro fabrication technique was presented to construct biocompatible, flexible, MRI compatible and micron size RF markers. Micro fabrication method is based on developing conductive paths and components using the shadow masking in physical vapor deposition (PVD), electroplating of conductive lines, and Parylene C coating process for some components and insulation commonly used to fabricate microsystems. Figure 2.3 expresses the outline of all main steps of the fabrication process. The solenoid coil, capacitor and conducting paths of the resonant RF marker, were fabricated using multiple layers on a non–planar catheter surface. Laser-cut cylindrical masks utilized as shadow masks during thin film coating in physical vapor deposition. Components of RC circuit appeared as thin film based solenoid coil, circular capacitor, and conductive paths. The parasitic capacitance caused by the intersection of the conductive lines combining the capacitor plate layers and solenoid coil turns was also taken into account to determine the required capacitor plate dimension for RF marker.

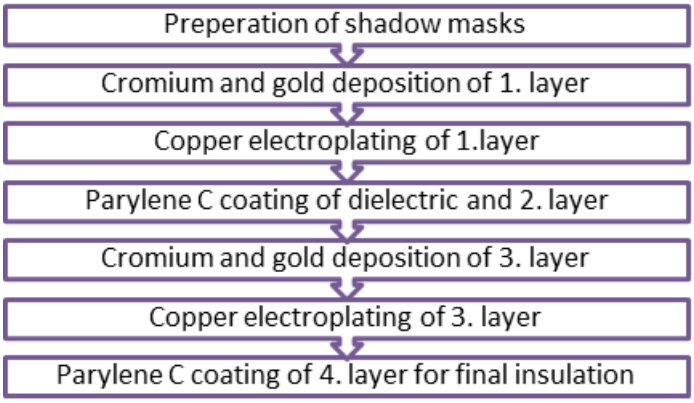

Figure 2.3 Outline of the fabrication process of RF marker.

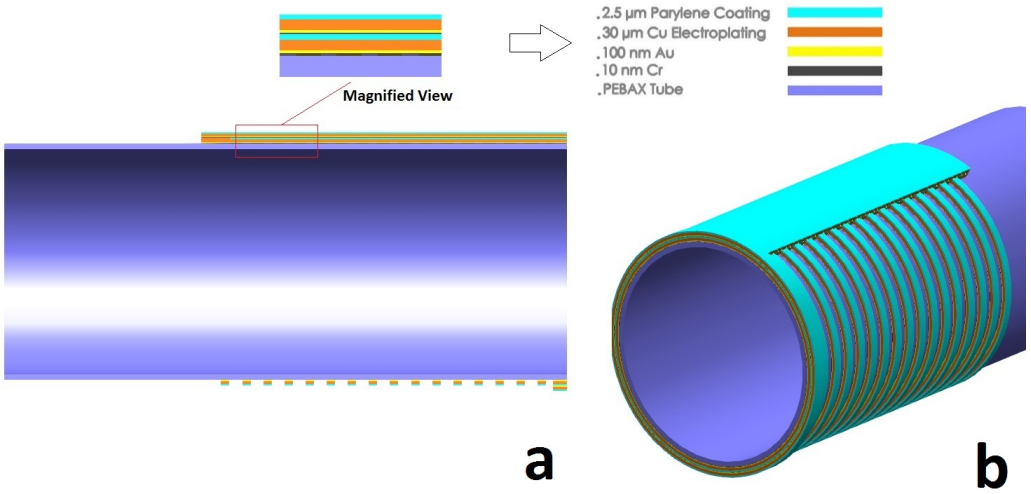

Figure 2.4 Computer aided design drawings of the fabricated RF marker (not to scale). a) Cross sectional view and magnified views of RF marker showing thickness of thin film layers deposited on cylindrical catheter tube (Pebax). b) Overall view of RF marker including all layers.

2.1.3 Preparations of Shadow Masks

Shadow mask geometries were designed using computer aided design (CAD) software (Pro-Engineer Creo 2.0) and converted to G codes by post processing software (Alpha CAM). The cylindrical masks were manufactured using a 4 axis Nd:YAG laser-cutting system (JK 400, P.A.L.S. Laser) from thin walled polyimide tubes (Figure 2.5). Both solenoid coil and capacitor plate layers are formed over the cylindrical catheter surface using these shadow masks.

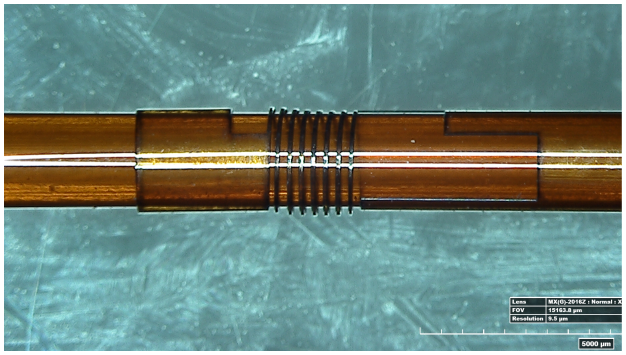

Figure 2.5 A combination of cylindrical and surface shadow mask prepared using a 4 axis Nd:YAG laser-cutting system (JK 400, P.A.L.S. Laser) from thin walled polyimide tubes.

2.1.4 Conductive Thin Film Formation through Physical Vapor Deposition (PVD) System

All conductive components of RF markers were constructed by deposition of chromium (Cr) (as an adhesion layer) and gold (Au) over a 5 Fr (1.67 mm) thermoplastic elastomer (Pebax) catheter shaft using a modified PVD system, high vacuum thermal evaporator (Figure 2.6). In general, PVD benefits a resistive heat source to evaporate a solid material in a vacuum environment to form a thin film. The conductive materials are heated in a high vacuum chamber until vapor stream coats the sample such as silicium (Si), titanium (Ti), aluminum (Al), silver (Ag), gold (Au) or etc.

Because PVD thin film deposition systems are designed to operate with planar surfaces such as silicon wafers, the target holder and rotation system to place cylindrical catheter shafts (up to three samples) were modified to enable continuous rotation of the holder during evaporation. The gear sizes and their tooth ratio were optimized to ensure each catheter shaft does not shadow the others and also rotate each holder at the same speed. The holders were made of metals so that, no outgassing occurred into the high vacuum environment ($\sim 3 \times 10^6$ Torr) during PVD deposition.

Figure 2.6 Outer view of utilized PVD thin film deposition system manufactured by NVTS, Nanovak, Turkey.

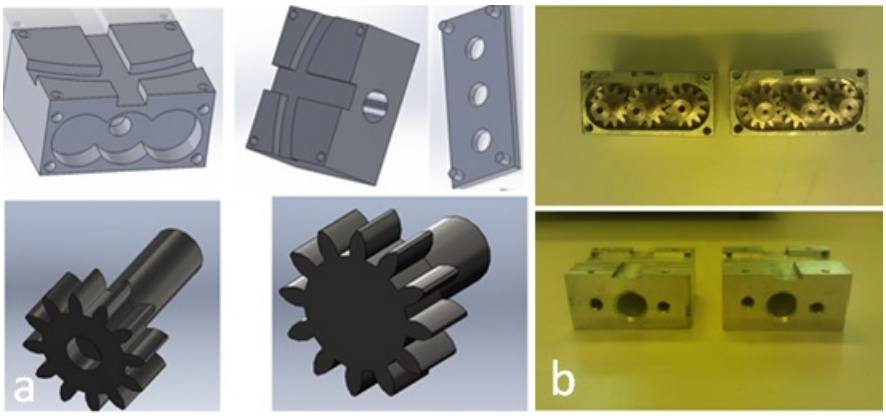

Figure 2.7 a) Target holder and rotation system drawings designed to place cylindrical catheter shafts (up to three samples) in "Solidworks" CAD program. b) Picture of fabricated 3 target holder prototype.

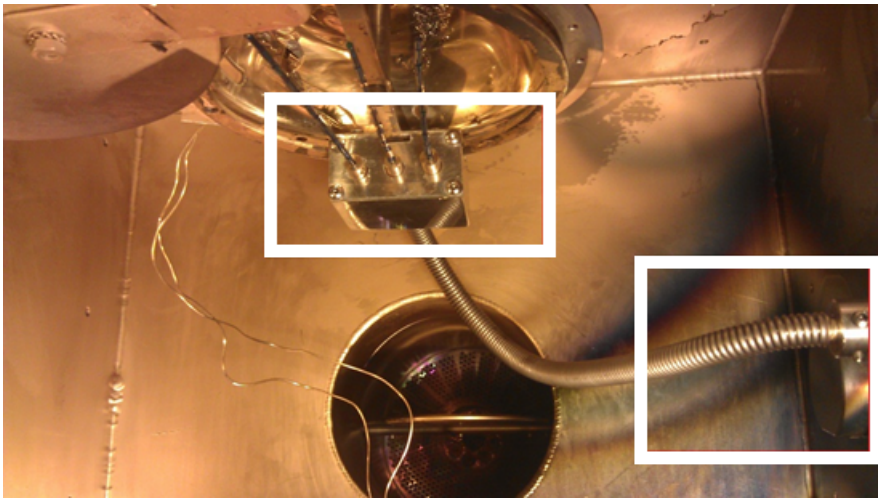

Figure 2.8 Chamber view of the PVD system. White color rectangles indicate the position of custom built target holder for 3 samples and rotation system.

In our experiment thermal deposition process starts with loading materials (a few gr chromium and 50 gr pure gold) that will be evaporated and coated over biocompatible Pebax samples. After the placement of the laser–cut masks over Pebax tubes, vacuum process lasts for 6 hours to ensure 3×10^6 Torr vacuum environment before the evaporation. In order to enhance the adhesion of gold material, first 10 nm chromium material can be coated over Pebax tubes. Then procedure gold material is coated with 100 nm thickness on surface of circular tubes. During both coating of chromium and gold materials, 3 samples are positioned by custom made holders that rotate around their axis at the same rotating speed.

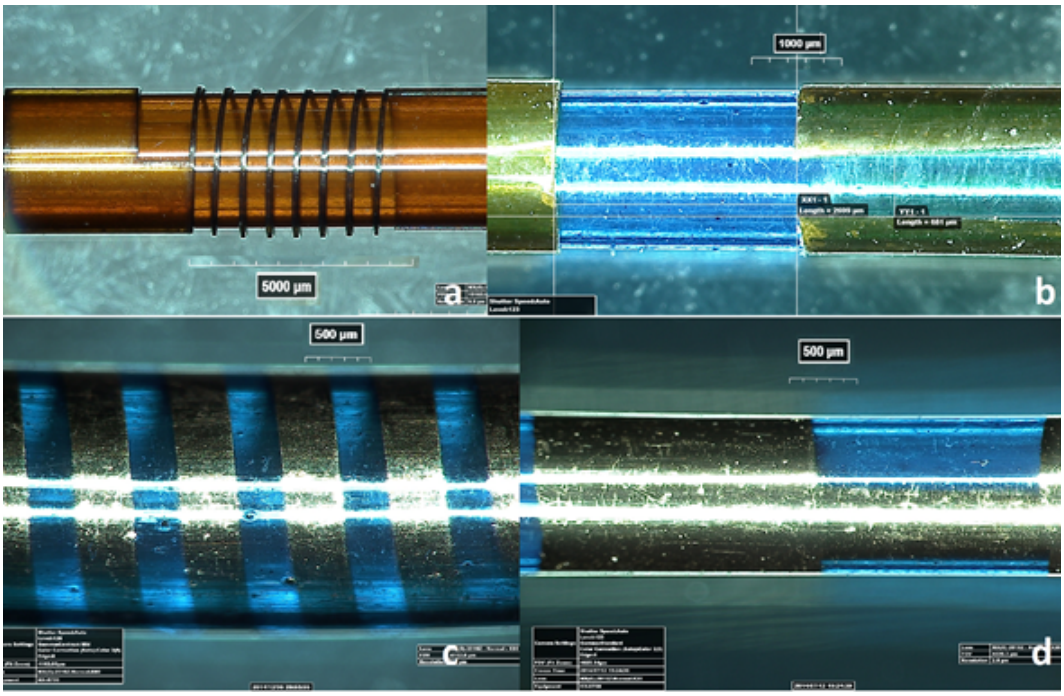

Figure 2.9 Thin walled polyimide shadow masks used to form a) solenoid coils and b) plate capacitors by PVD, The shadow masks were formed by a Nd:YAG laser-cutting process c) Magnified view (x80) of a thin film solenoid coil composed of Cr (10 nm) and Au (100 nm). d) Magnified view (x20) of a thin film capacitor plate coated with Cr (10 nm) and Au (100 nm).

2.1.5 Electroplating Process

The resistance (R) of the RF marker components depends on both the conductivity and coating thickness, which is limited by the skin depth observed at the MHz frequency range (Figure 2.6). Different from a straight cylindrical wire, the evaluation of skin depth is more complex for a helical coil due to the presence of electromagnetic fields from neighboring turns in the coil which alter the current distribution. In general, the proximity effect decreases the effective current-carrying cross-sectional area of the coil [79] and increases the value of R. However, as the thickness of the deposited metal increases, R of the coil decreases, and remains constant.

Figure 2.10 Electroplating setup including cupper electroplating solution bath, heater and power supply together with multimeter for sensitive measurement of applied current.

Electroplating is an electrochemical deposition process used to produce a dense, uniform, and adherent coating, usually of a metal or alloy, on a conductive surface by the act of electric current [108]. Copper electroplating process was performed over the deposited solenoid coil, capacitor plates and interconnection lines to increase the conductive layer thickness and to lower the overall resistance (Figure 2.11, 2.12). The electroplating solution was composed of copper sulfate as a metal source, sulfuric acid, and hydrochloric acid as catalysts, and water. Solution uniformity was maintained by magnetic stirrer at the bottom of the bath. The electroplating solution temperature and conductivity was monitored to provide each layer was 30 μm thick (Figure 2.10).

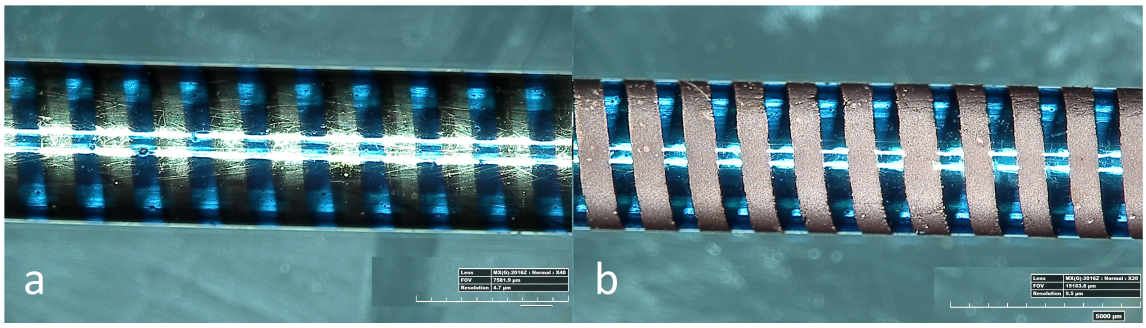

Figure 2.11 a) image indicates the gold material coated solenoid coil before electroplating process. b) image indicates the solenoid coil after 15 minutes electroplating process.

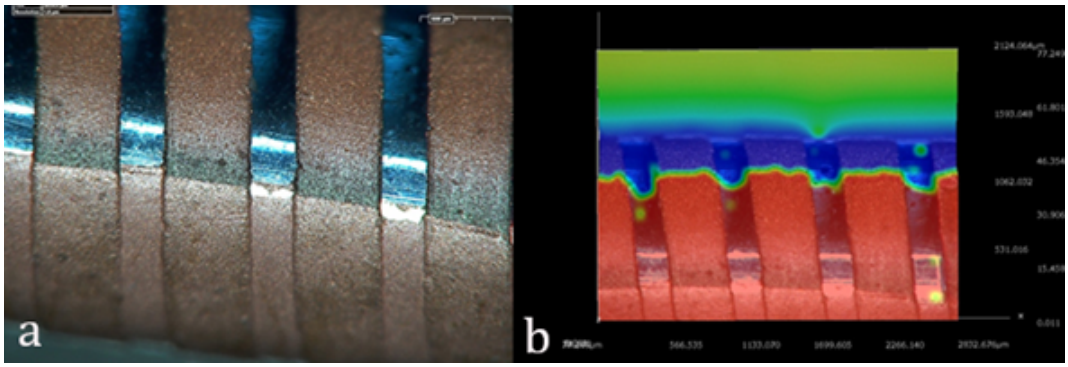

Figure 2.12 a) Magnified image (x50) of solenoid coil layer and conductive path after electroplating process. b) 3D topographic image and thickness measurement of electroplated layers. Images were obtained by Hirox KH-8700 microscope.

2.1.6 Parylene Coating Process

Parylene C (Dimer DPX-C, SCS Equipment) was used as a dielectric material between the conductive layers of the RF marker and also as the final insulating layer. The coating process was performed using a Parylene deposition system (Labcoater 2-PDS 2010, SCS Equipment) with Parylene C (5 g) in a standard procedure to achieve a uniform coating thickness of 2.5 μm (Figure 2.13).

The thickness of the deposited conductive layers and Parylene C was determined by using a surface profiler (Dektak XTL, Burker) which was able to measure the coating thickness in nanometers (Figure 2.14).

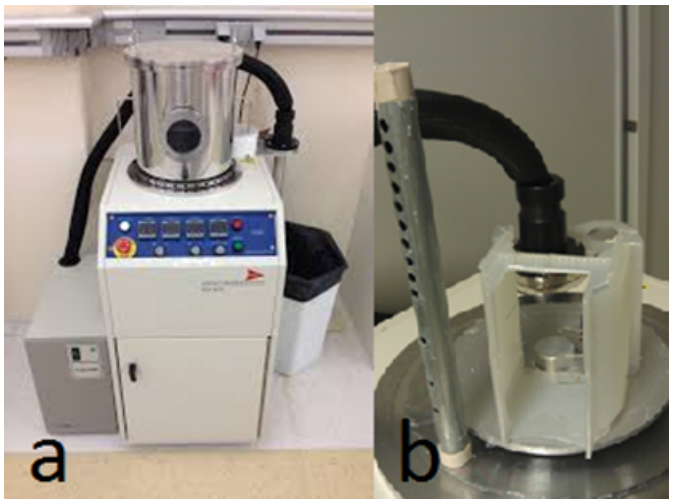

Figure 2.13 a) Parylene C coating device (Labcoater® 2-PDS 2010, SCS Equipment). b) Inner view of the Parylene C coating device.

Figure 2.14 Representative measurement of the final isolating layer thickness (2.5 μm) of Parylene C using a surface profiler (Dektak XTL, Burker).

2.1.7 Resonant Frequency Evaluation of RF Markers

The L and C values of the RF resonant markers were tested using vector network analyzer (ZVL3 Vector Network Analyzer, Rohde-Schwarz). Conductive silver epoxy (5000 Silver Conductor, DuPont) was used to provide electrical contact for the probes throughout the measurements.

The resonance frequency of the resonant marker prototypes were measured by using a custom design non–contact sniffer probe with an eigen frequency of around 162 MHz. The non–contact sniffer probe was constructed using a 20 cm long, 50 ohm semi rigid coax cable. For proper measurement, calibration of the sniffer was performed using a short circuit probe, open circuit probe, and 50 ohm matching probe at the same length (Figure 2.15).

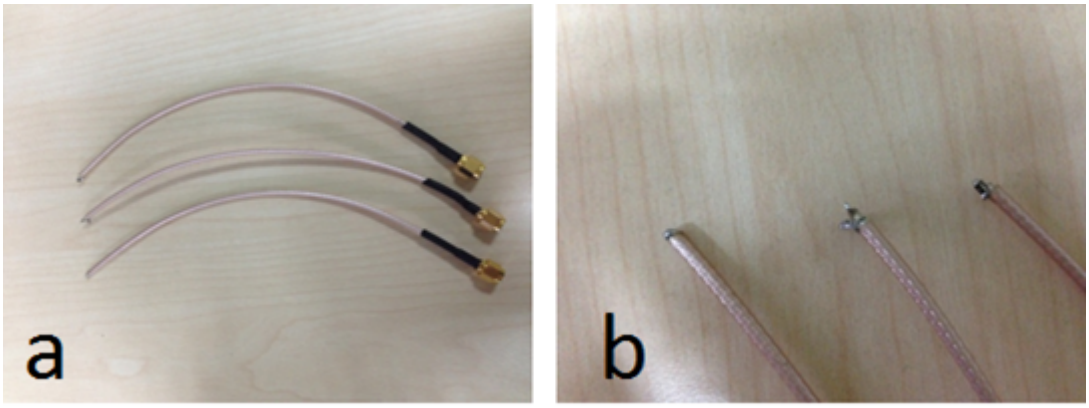

Figure 2.15 a) A short circuit probe, open circuit probe, and 50 ohm matching probe at the same lengths for calibration before the measurement of resonant frequency of RF circuit. b) Magnified view of short circuit probe, open circuit probe, and 50 ohm matching probe that indicates tip of regarding probes.

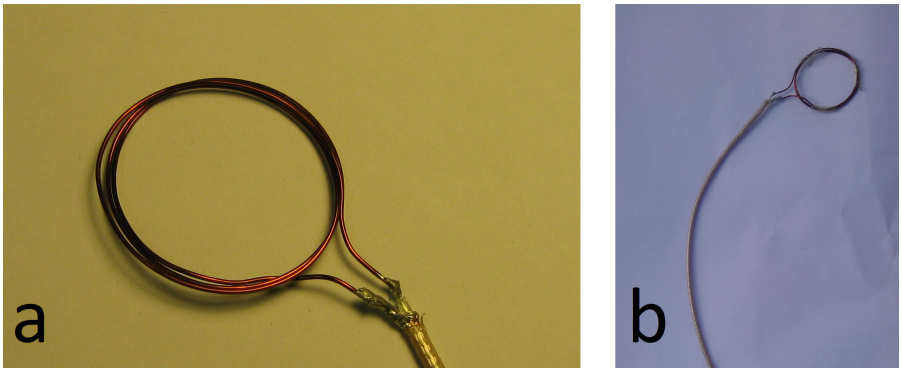

Figure 2.16 a) Magnified picture of a custom design non-contact sniffer probe tip b) Overall view of manufactured non–contact sniffer probe with an eigen frequency of around 162 MHz.

2.1.8 Integration of RF Markers with 5 Fr Guiding Catheter

Interventional clinical applications need more than a meter long catheters in order to be navigated through vessels and cardiac chambers by interventionists. Therefore

fabricated RF markers need to be combined with long and deflectable catheter shafts. The constructed RF marker was attached into the 150 cm long biocompatible 5 Fr (1,67 mm) Pebax polymer tube by using thermal process (Figure 2.17).

First of all the proximal catheter shaft was constructed by covering 0.96 mm (inner diameter) polytetrafloroetilen (PTFE) tube over a Parylene C coated steel mandrel liner. After that the distal RF marker and long catheter shaft was linked to each other by heat shrink tubing (FEP - fluorinated ethylene propylene material tube). For clinical procedures a standard hub was attached to the proximal side using medical grade glue (Dymax Corporation Cath 200A) that activated by UV radiation.

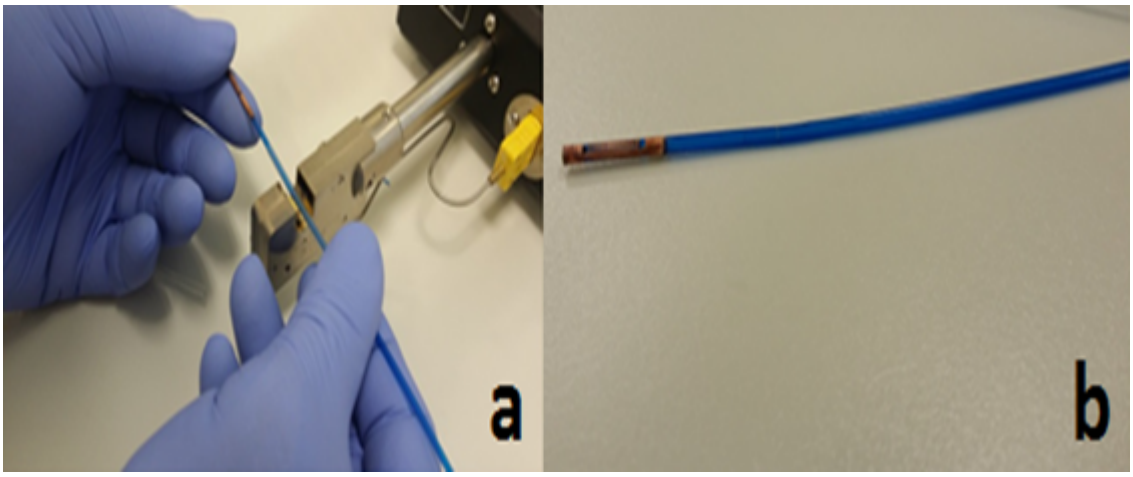

Figure 2.17 a) Image of fusing of a RF marker to the catheter shaft. b) Overall catheter with a RF marker at distal tip after process.

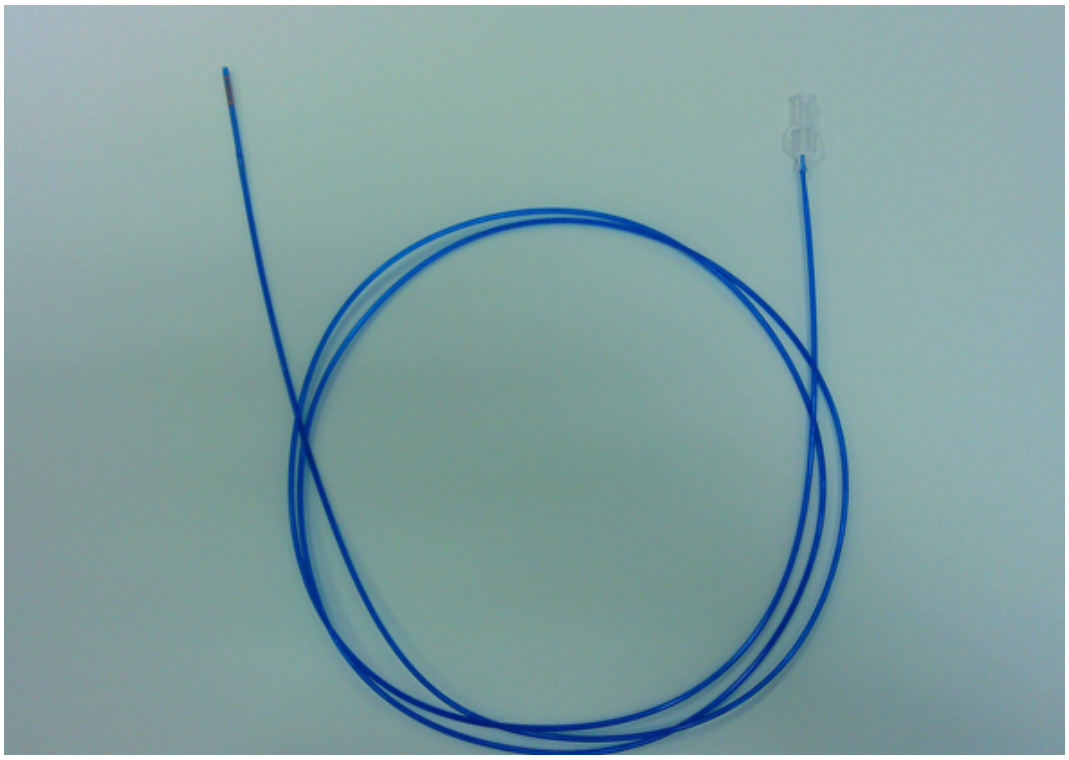

Figure 2.18 View of 150 cm long deflectable, biocompatible and MRI compatible entire catheter including RF marker at distal and standard hub at proximal.

2.2 RF Coil Design Simulations in Comsol Multiphysics

In this part of the thesis, an orientation independent simulation model was constructed to evaluate the visibility performance of different RF marker designs in MRI environment. Delineating a virtual platform for testing RF marker prototypes with different orientation according to standard birdcage coil helps to analyze the induced electromagnetic field, homogeneity distortion and B_1 field circularity in the volume of interest.

2.2.1 Simulation Workflow

For setting up and solving a simulation model in Comsol Multiphysics 5.3, it is necessary to follow a standard workflow. Sequence of steps for a standard workflow was expressed below;

- Setting up a model environment
- Creating a geometry
- Specifying materials and their properties
- Defining physics and boundary conditions
- Creating a mesh
- Running simulation
- Postprocessing results

By following the regarding steps, we set up our simulation model, and evaluated the results according to our assumptions.

2.2.2 Validation of Finite Element Modeling of a Birdcage Coil

RF birdcage coils have become widespread in the field of MRI imaging. Their simplicity in design followed by a high homogenous magnetic field due to continuous sinusoidal current distribution on the surface of the coil led to their popularity. Modeling the birdcage coil in a 3D simulation environment helps to examine the electromagnetic field in the volume of interest, such as field homogeneity, B_1 field circularity [109]. Starting point of the simulation model studied in this thesis was an available model in COMSOL Multiphysics model. Finite Element Method (FEM) model of low-pass birdcage coil in order to obtain a homogenous magnetic field and circular B_1 field inside the birdcage coil in 3 Tesla MRI was already prepared and shared by program supplier[110]. In this study, prepared model for 3 Tesla MRI, was modified and made suitable for 1.5 Tesla MRI scanner. Similar conditions was set up and evaluated for 1.5 Tesla MRI environment.

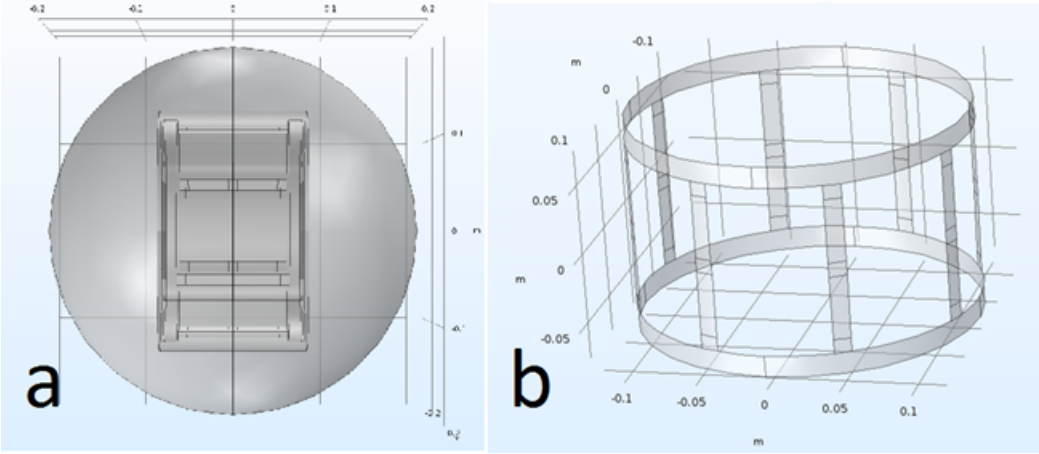

Figure 2.19 a) Geometric model of whole MRI virtual platform b) Geometric model of a low-pass birdcage coil inside MRI environment.

Geometric parameters of custom designed low-pass birdcage coil;

- Radius of the sphere : 20 cm
- Radius of the birdcage coil : 12 cm
- Height of the birdcage coil : 15 cm
- Length of the capacitive elements : 1 cm
- Number of the capacitive elements : 22
- Number of the legs : 8
- Number of the activation ports : 2

In order to validate the designed MRI platform, a phantom was placed into the middle of the model that has the similar properties with ASTM F2182 phantom (Relative permittivity: 80, relative permeability: 1, electrical conductivity: 0.47 S/m). Electric field distribution on the surface and the volume of the constructed phantom was compared with previously reported electric field distributions in the ASTM phantom [111].

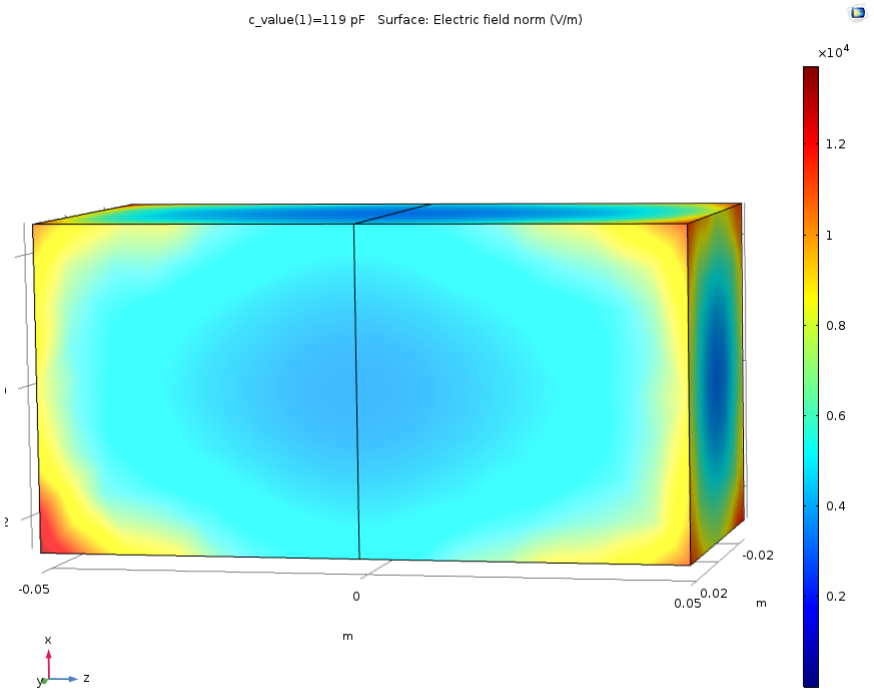

Figure 2.20 The phantom that simulates a saline water filled tank with 5 cm width, 5 cm depth and 10 cm length.

2.2.3 Quadrature Excitation in Frequency Domain Analysis

As mentioned in former section, first part of our simulation studies was inspired by thesis studies [109,110] that utilized program of Comsol Multiphysics while inspecting effects of varied conditions, and parameters of instruments in MRI scanner environment. According to these studies, in order to effectively design a birdcage coil, capacitance tuning is necessary to determine optimum capacitance value to obtain homogenous magnetic field distribution. In the simulation process, frequency domain analysis was used to find the optimal capacitance value at the Larmor frequency. Lumped ports were used to provide quadrature excitation. For low-pass birdcage coil, capacitors were placed accordingly to the type of coil to determine the resonant frequency and the uniformity of the field it produces. Boundary conditions were assigned to the surface of the coil elements and the outer boundary of the solution domain enclosing the coil geometry. Scattering boundary conditions were also used to avoid any electromagnetic wave reflection back to the coil. The coil surface and the RF shield

around the coil were assigned the perfect electric conductor (PEC) condition. Firstly air domain was used to study the performance of the low-pass birdcage coil. The homogeneity was attained by quadrature excitation and optimal capacitance values of lumped elements in the coil.

COMSOL Multiphysics allows us to specify more than one frequency in order to observe the variation of any electromagnetic field parameter with respect to the frequency. For instance, the return loss (S_{11}) can be inspected by running simulations for a range of frequencies (frequency sweep) to see where smaller return loss is occured within specified capacitance value. In order to obtain both homogenous and circularly rotating B_1 field at the desired frequency, the capacitance was tuned by using the parametric sweep. The circularity of the field was evaluated by estimating the axial ratio of the magnetic field around the air phantom while the homogeneity of B_1 field, was calculated using the standard deviation of the electric field around phantom.

In the frequency domain analysis, quadrature excitation was used to obtain homogeneous and circularly-polarized magnetic field in the birdcage coil by tuning the capacitors properly. Quadrature excitation was driven from two ports which are equal in magnitude but with a phase of 90° to generate circularly-polarized field inside the coil. Quadrature excitation generates circularly polarized field which is more homogeneous than linear excitation as a result of equal currents distribution along the legs of the coil. In addition, quadrature driven birdcage coil is more power efficient compared with linear drive, by reducing the RF power requirement by a factor of two.

$$B_{linear} = B_1 \cos(\omega t)x = (B_1^+) + (B_1^-) \tag{2.10}$$

where

$$B_1^+ = \frac{B_1}{2}(\cos(\omega t)x \pm \sin(\omega t)y) \tag{2.11}$$

The first term represents a right-circularly polarized field while the second term represents left-circularly polarized field having equal magnitude of $B_1/2$.

2.2.4 Simulating The Low-Pass Birdcage Coil with The RF Marker Prototype

For the air phantom, excellent magnetic field homogeneity and B_1 field circularity were maintained. Adding to that it is necessary to check the alternation through the magnetic field homogeneity and B_1 field circularity when the RF marker coil is placed into the low-pass RF birdcage coil in MRI. Therefore, the same analysis was applied while the designed RF coil marker was placed at the center of the low-pass birdcage coil domain. First optimum capacitance value was observed for the altered domain at the Larmor frequency. Secondly the effect of designed RF marker was examined with respect to the RF field homogeneity and B_1 field circularity.

First of all, precise geometry of the fabricated RF marker prototype was built in model by using drawing tools in Comsol Multiphysics. Both geometric parameters of sketched RF marker and properties of materials defined in Comsol Multiphysics, completely identical with the RF marker prototype implemented in laboratory studies (Figure 2.21).

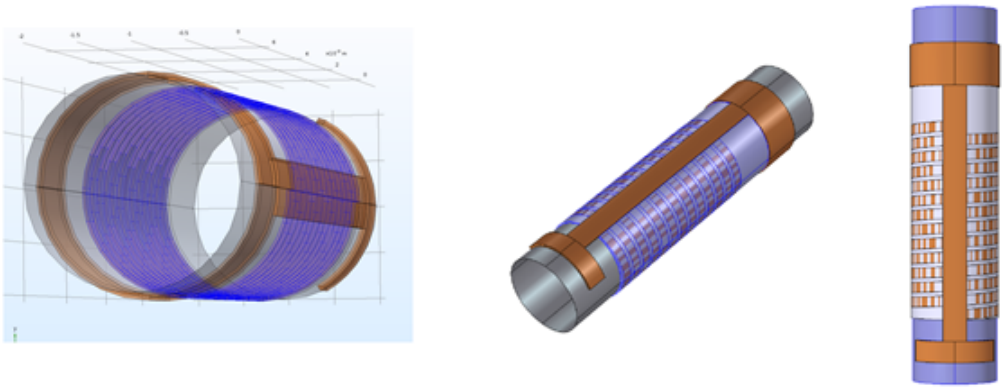

Figure 2.21 Dimensions of defined RF marker; radius: 1mm, number of turns of coil: 13, thickness of coil, capacitor plates and conductive layers: 30 μm, thickness of dielectric substance (parylene C): 2.5 μm.

2.2.5 RF Coil Designs for Semi–Active Markers

2.2.5.1 Helical Coil Design . In this part of this thesis, different RF coil in RF marker designs were performed to evaluate their performance into the birdcage coil in MRI platform. Figure 2.22 indicates one helical coil that can be used as a coil in a RF marker.

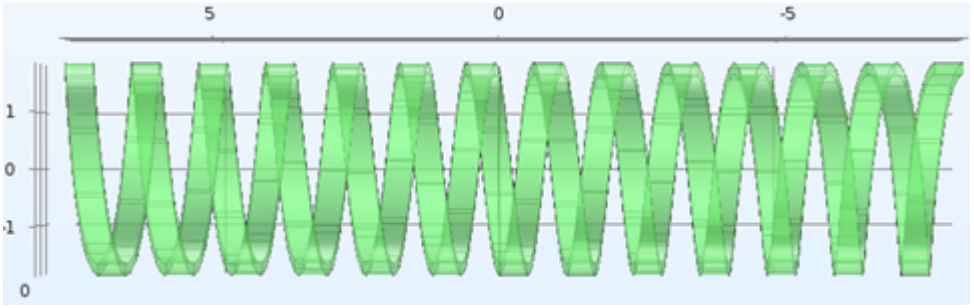

Figure 2.22 Image indicates designed helical RF coil.

Geometric parameters of custom designed helical RF coil;

- Diameter of the RF marker coil : 1.67 mm
- Length of the RF marker coil : 5 mm
- Number of the turns of the RF marker coil : 13
- Pitch between the two coil turns (wp) : 100 μm
- Width of the each coil turn (ww) : 200 μm

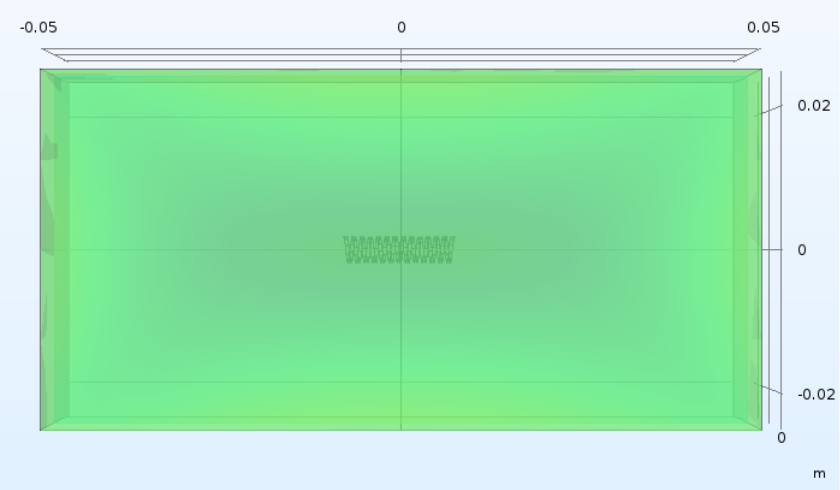

Figure 2.23 Image indicates designed helical RF coil placed into ASTM phantom that simulates a saline water filled tank with 5 cm width, 5 cm depth and 10 cm length.

2.2.5.2 Double Helical Coil Design. Figure 2.24 indicates double helical coil that can be used in a RF marker.

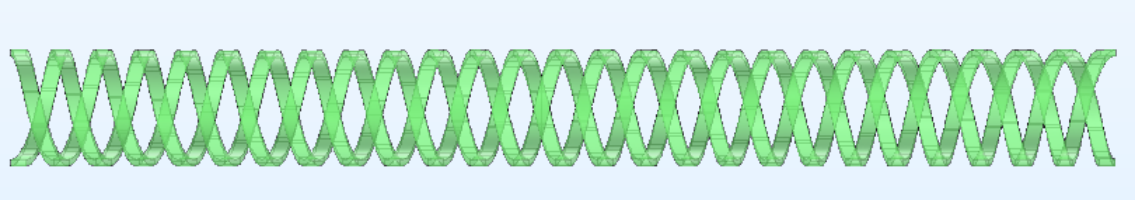

Figure 2.24 Image indicates designed helical RF coil.

Geometric parameters of custom designed helical RF coil;

- Diameter of the RF marker coil : 1.67 mm
- Length of the RF marker coil : 2.5 cm
- Number of the turns of each coil : 13

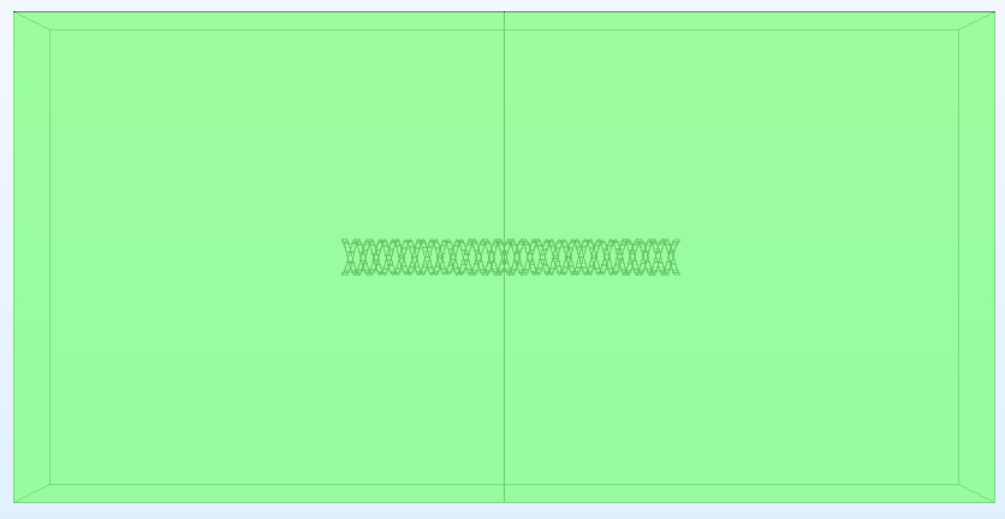

Figure 2.25 Image indicates designed double helical RF coil placed into ASTM phantom that simulates a saline water filled tank with 5 cm width, 5 cm depth and 10 cm length.

3. RESULTS

The profile of the RF markers was decreased by more than 78 %, compared with that of commercially available MRI compatible circuit components. Moreover, the RF markers provided satisfactory visibility performance under various orientations relative to B_0. Heating tests confirmed that the embedded RF marker does not pose a heating risk. In the following sections these criterias will be presented in details for one of the manufactured ideal RF marker prototype.

3.1 Comparison of Theorical Calculations and Experimental Measurements

Fabricated RF marker incorporates 4 different thin film layers including conductive coil layer, circular plates of capacitor, conductive path for interconnection between coil and capacitor, parylene coating layers as dielectric and as an insulator. Since even the thickest layer of the coatings is lower than the 30 μm, all steps of the micro fabrication needs to be in accurate set up and processing. Unfortunately a simple displacement of a shadow mask during the thermal evaporation or extra electroplating of a conductive layer or inhomogenity on parylene dielectric coating may be result with significant differentiation at inductance or conductance value. And finally that result in a distinctive shift in resonance frequency of the designed RF marker.

Since precise inductance, capacitance and resonance frequency values are the key factors for determining the characteristics of the RF marker including SNR, Q factor and SAR, all micro fabrication steps have to be applied with specific procedures. As it can be seen in Table 1, numerous RF markers with various parameters manufactured during this study. After several trials, it is achieved to minimize experimental errors and to obtain almost ideal RF markers prototypes that supply satisfying performance characteristics. All of the measurements and evaluations mentioned in the following sections were collected from one of the ideal RF marker prototype [RF Marker 7].

Table 3.1
Comparison of calculated and measured parameters of RF marker prototypes.

# of RF Marker	Coil radius (mm)	# of turns	Coil length (mm)	L (nH)	Contact C(pF)	Circular C (pF)	Total C (pF)	Reson. Freq. in Air (MHz)	Measured Reson. Freq. in Air (MHz)	Reson. Freq. in Saline Water (MHz)
RF Marker 1	1	4	1.55	28.4	6.3	213	219	63.8	*	*
RF Marker 2	1	6.5	4.64	24.3	14.4	258	272	61.9	59	*
RF Marker 3	0.835	15	9.6	64.2	25.1	69.2	94	64.7	70.7	69
RF Marker 4	0.835	14	9	60	25.1	75.8	101	64.6	62	60
RF Marker 5	0.835	13	8.2	55.9	25.1	75.8	101	67	64.7	63.6
RF Marker 6	0.835	26	16.9	110	109	0	109	64.7	74.2	70.7
RF Marker 7	0.835	13	4.45	59	24.7	78	103	64.7	64.3	63.86

3.1.1 Evaluation of an Ideal Manufactured RF Marker Prototype

The measured inductance value (60 nH) for the solenoid coil was consistent with the calculated value (59 nH). The reason of this acceptable differences might be alteration at coil turn width (ww), turn pitch (wp) and turn thickness (wt). For instance according to the detailed measurements collected from one of the RF markers, coil turns widths change between 208 μm and 255 μm instead of 250 μm. Similarly turn pitch of the coil vary from 94 μm to 103 μm, instead of 100 μm.

On the other hand the measured capacitance of the capacitor showed 5 % deviation from the theoretical value. This deviation was probably caused by using a simplified equation (Equation 2.5) for contact capacitance calculation between the conductive line (interconnection between solenoid and capacitor) and solenoid coil turns. This deviation ultimately imparts 2 % difference between the calculated and measured resonance frequency of the RF markers.

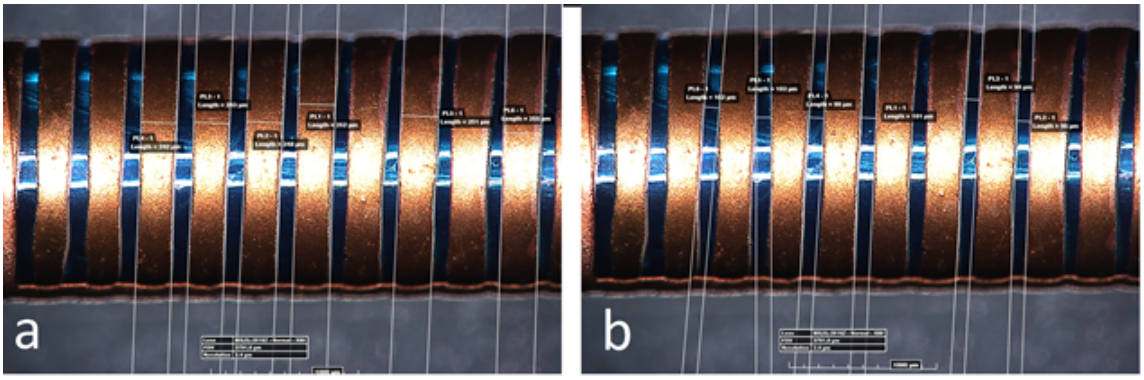

Figure 3.1 Measurements related with coil turns such as ww (wire width), wp (winding pitch) by using Hirox KH-8700 microscope.

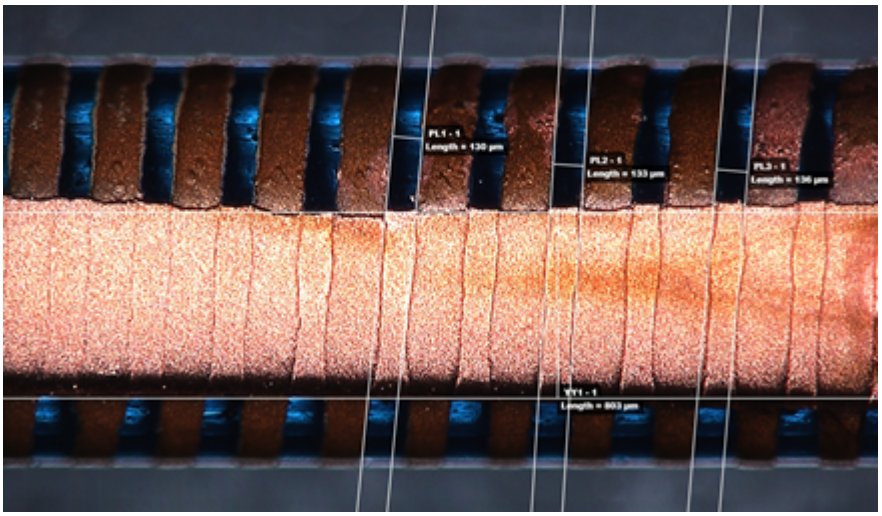

Figure 3.2 Image indicates interconnection path between thin film capacitor and thin film coil located in different layers.

Despite these minor errors, a semi–active RF marker was fabricated that was tuned at 63.8 MHz, which is the Larmor frequency of 1.5 T MRI.

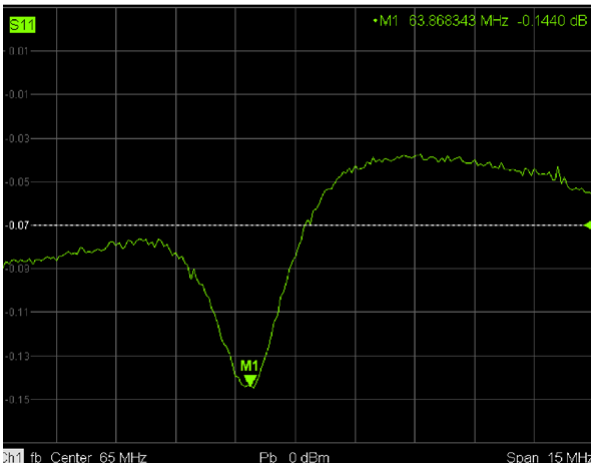

Figure 3.3 Resonant frequency measurements of RF markers by using a non–contact RF search probe connected to the network analyzer. Signal drop expresses the tuned frequency (63.8 MHz) for the S_{11} signal.

The resonant frequency and sensitivity of the resonant markers were measured through S_{11} measurement in a sniffer probe. Measurements were carried out into 0.9% saline solution to mimic the conditions of the human body. Attenuated reflection at the desired frequency (63.86 MHz) in 0.9% saline medium is illustrated in Figure 3.3.

3.1.2 Visibility Test of RF Marker under MRI

The visibility performances of RF markers were tested in a 0.9% saline water-filled phantom with dimensions of 40 x 50 x 17 cm. The GRE sequence (TE/TR = 2.3/969 ms, flip angle = 5°) was utilized for imaging the RF marker under 1.5 T MRI (Tesla Espree Model Siemens MRI, located at Kozyatagi Hospital Istanbul, Turkey). The catheter distal tip was oriented parallel, perpendicular and 45° to the main magnetic field to evaluate the orientation dependence of the received SNR of the RF marker (Figure 3.4).

Figure 3.4 Image of the MRI set up utilized for imaging the RF marker under 1.5 T MRI (Tesla Espree Model Siemens MRI, located at Kozyatagi Hospital Istanbul, Turkey).

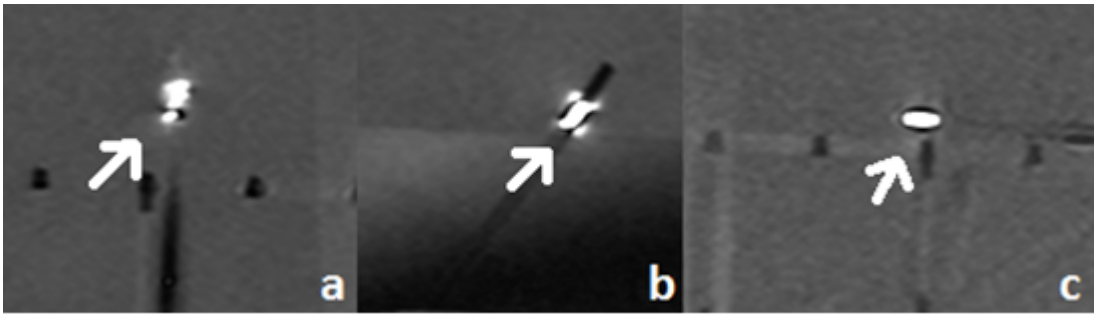

Figure 3.5 The RF marker appeared as a "bright spot" (indicated by white arrows) under MRI 1.5 T. Images show the MRI visibility of the RF marker when placed parallel to the main magnetic field B_0, b) oriented 45° relative to Bo, and c) placed perpendicular to B_0.

The inductive coupling between the semi–active RF resonant marker and the surface coil of the MRI scanner provided satisfactory distal tip visibility for different catheter orientations relative to B_0 under 1.5 T MRI (Figure 3.5).

3.1.3 RF Heating and Safety Performance Test under MRI

A RF induced heating test of 5 Fr guiding catheter (>150 cm Pebax polymer tube) prototype with the RF marker at its distal tip was performed in an acrylic phantom that simulated the electrical and thermal properties of the human body. A fiber optic thermometry probe (Opsens Inc.) was placed at the distal end of the solenoid coil of the RF resonant marker where the heating induced by B1 was expected to be the greatest. The distal end of the catheter (where the RF marker was located) was aligned perpendicular to the main magnetic field (B_0) that is assumed the worst case orientation, 9 cm vertical offset from the phantom bottom, and 12.5 cm horizontal offset to the iso center.

A RF field producing a sufficient whole body averaged SAR of about 2 W/kg averaged over the volume of the phantom was applied for approximately 15 min. with a True FISP sequence (TE/TR =1.3/30 ms, flip angle = 66°) in compliance with standard ASTM F 2182-11a. The maximum temperature rise was recorded as 0.35°C. The RF induced heating risk arises when the electrical length of the metal components of an interventional device exceeds the quarter wavelength length in a body. This is approximately 12 cm for a 1.5 T scanner. Our RF resonant marker is 5 mm long, which is much shorter than this critical length [112]. In addition, our heating test results showed that the temperature rise caused by the RF resonant marker was acceptable (0.35°C), and within the FDA allowed limit for the torso area (Zalenga, 2001).

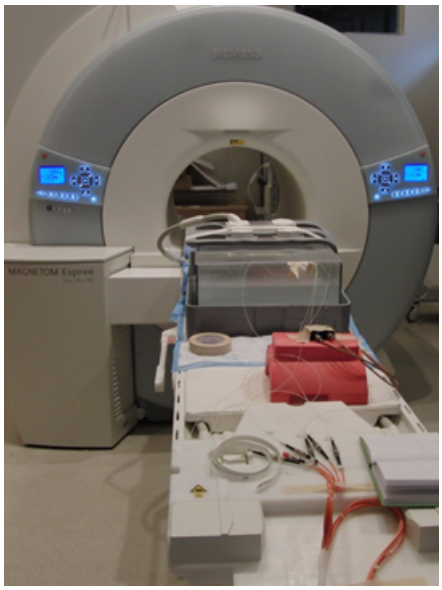

Figure 3.6 Image of the MRI set up utilized for RF induced heating test of RF resonant marker under 1.5 T MRI using a fiber optic thermometry probe (Opsens Inc.).

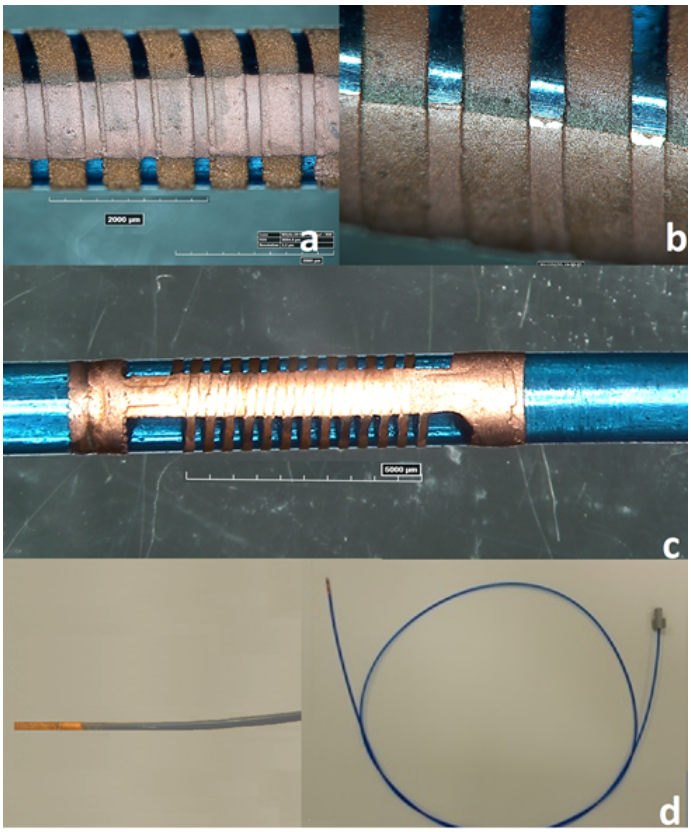

Figure 3.7 a) Final multi layers (coil and intersection of conductive layers) view of the RF marker after electroplating. A return path (horizontal stripe) which is separated from the solenoid by an insulating layer enables interconnection between the solenoid and capacitor. b) Magnified view (x120) of the multi layers. c) Overall view of the RF marker with all components. d) Photographs of the distal tip (left) guiding catheter (right).

3.2 Simulating The Low-Pass Birdcage Coil without The RF Marker Prototype

3.2.1 Capacitance Tuning Using Parametric Sweep

The designed birdcage coil have an inductor and many capacitors that have to resonate at the Larmor frequency of regarding MRI scanner. Initial tuning began by calculating the capacitance value, which is necessary for the coil to resonate at the desired frequency (63.8 MHz). Optimum capacitance value can be found by tuning the capacitor using a function name is parametric sweep. The capacitance values range from 120 pF to 130 pF with a step capacitance of 0.5 pF were applied at 63.8 MHz. The air phantom has a material property of electrical conductivity $\sigma = 0$ S/m, relative permeability $\mu_r = 1$ and relative permittivity $\epsilon_r = 1$.

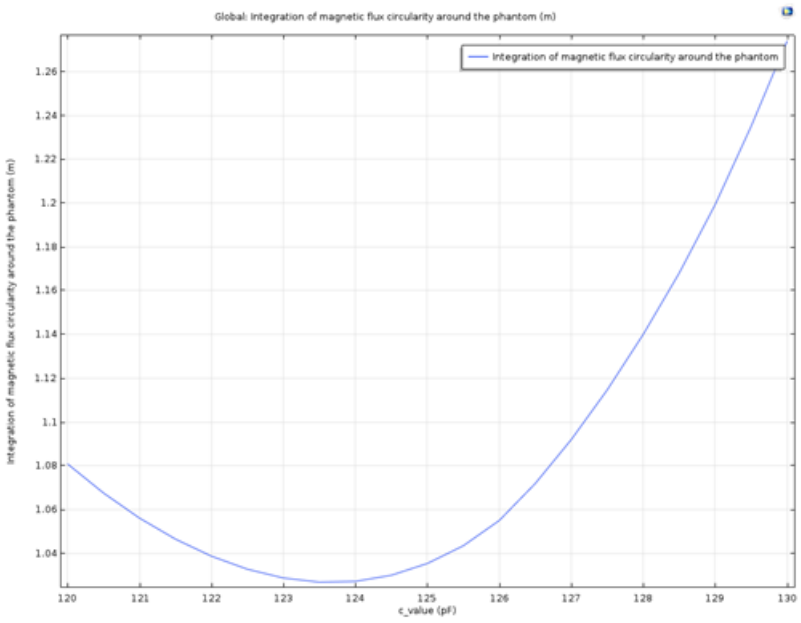

Figure 3.8 The axial ratio of the magnetic flux density for coil at 63.8 MHz.

.

The homogeneity of the field is calculated by using the standard deviation of the electric field. As it can be seen from Figure 3.9, the optimal value of the capacitance is close to 123.5 pF.

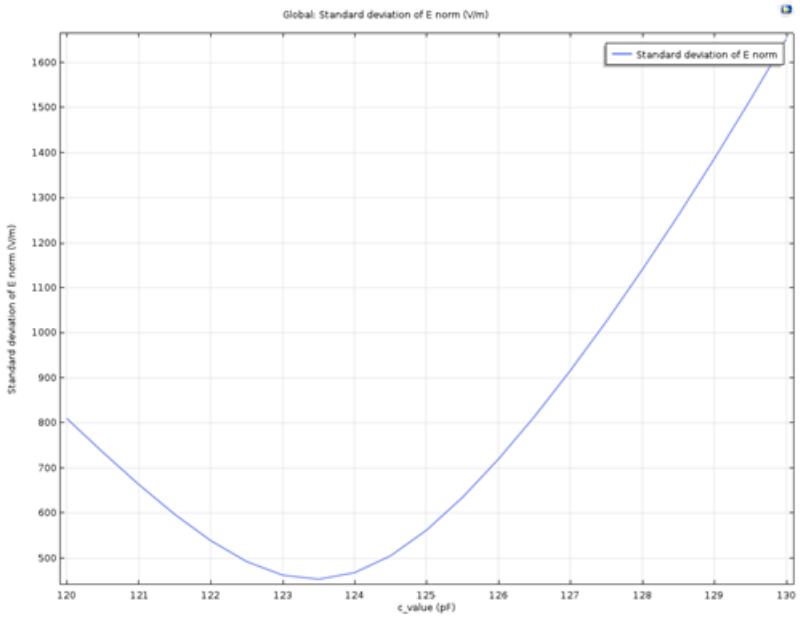

Figure 3.9 The standard deviation of the electric norm for coil at 63.8 MHz (Larmor frequency of 1.5 Tesla MRI).

.

3.2.2 Magnetic Field Homogeneity Evaluation of the Low-Pass Birdcage Coil

In order to evaluate the magnetic field homogeneity of the low-pass birdcage coil, a simulation was carried out for 8-leg low-pass birdcage coil loaded with air phantom as inspired studies mentioned before [109,110]. Capacitance value used on the rungs was 123.5 pF and the simulation frequency was 63.8 MHz. A homogenous magnetic field around the air phantom at 63.8 MHz was shown in Figure 3.10.

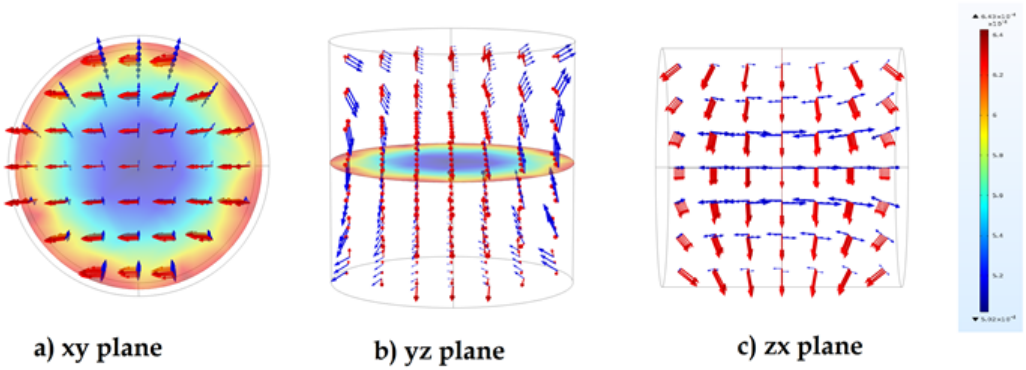

Figure 3.10 Magnetic flux density distribution with real (red) and imaginary (blue) part of the magnetic flux density for coil at 63.8 MHz. a) indicates xy plane, b) indicates yz plane, c) indicates zx plane [109,110]

.

3.3 Simulating The Low-Pass Birdcage Coil with The RF Marker Prototype

3.3.1 Capacitance Tuning Using Parametric Sweep with The RF Marker

Similar to the low-pass birdcage coil model without RF marker, optimum capacitance value was found by tuning the capacitor using a parametric sweep when designed RF marker was placed at the center of low-pass birdcage coil. The capacitance values range from 120 pF to 130 pF with a step capacitance of 0.5 pF were applied at 63.8 MHz

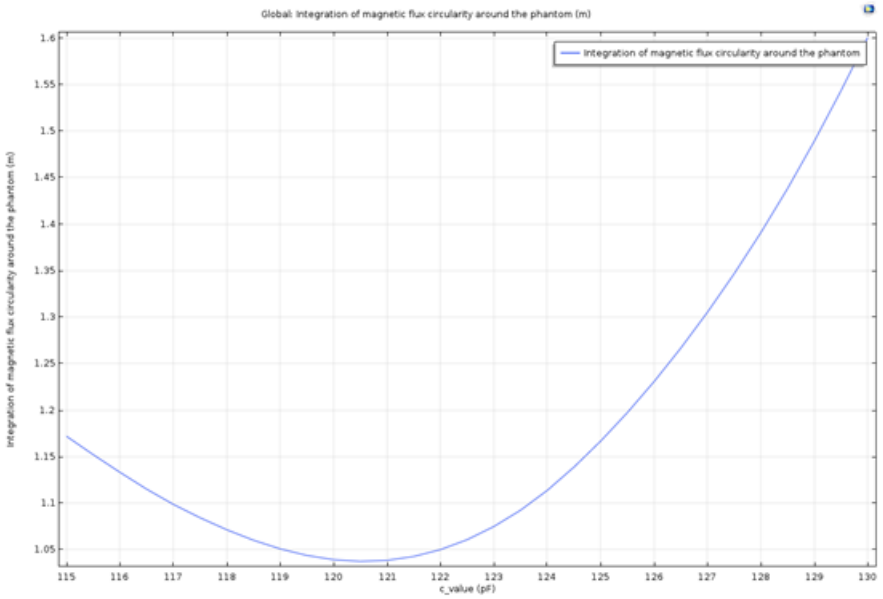

Figure 3.11 The axial ratio of the magnetic flux density for coil with the RF marker at 63.8 MHz (Larmor frequency of 1.5 Tesla MRI).

.

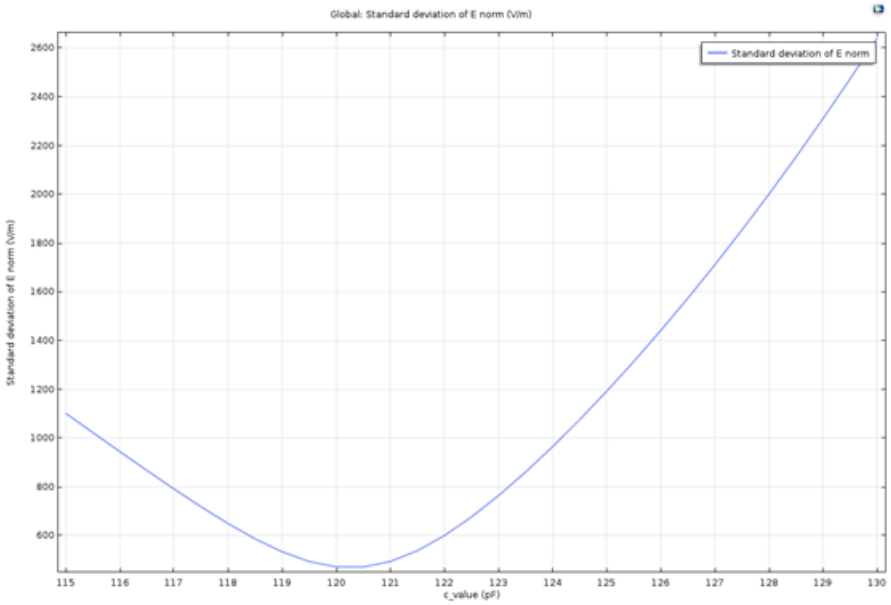

Figure 3.12 The standard deviation of the electric norm for coil with the RF marker at 63.8 MHz (Larmor frequency of 1.5 Tesla MRI).

.

3.3.2 Magnetic Field Homogeneity Evaluation of the Low-Pass Birdcage Coil with The RF Marker

In order to analyze the effect of RF marker on magnetic field homogeneity, the simulation was run for 8-leg low-pass birdcage coil loaded with air phantom and RF marker prototype. Capacitance value used on the rungs was 120.5 pF and the simulation frequency was 63.8 MHz. A homogenous magnetic field both around the air phantom and RF marker at 63.8 MHz was shown in Figure 3.13.

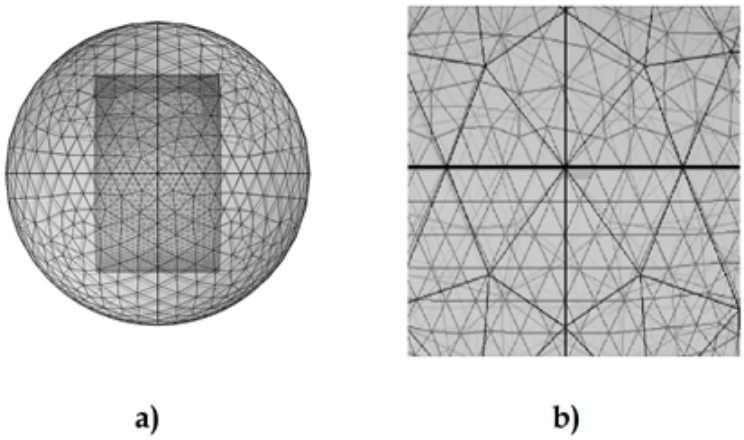

Figure 3.13 a) View of mesh structure on whole MRI environment, low-pass birdcage coil and RF marker. b) Magnified view of mesh structure. (to visualize RF marker in low-pass birdcage coil). Radius of the sphere that simulates MRI environment is 20 cm.

.

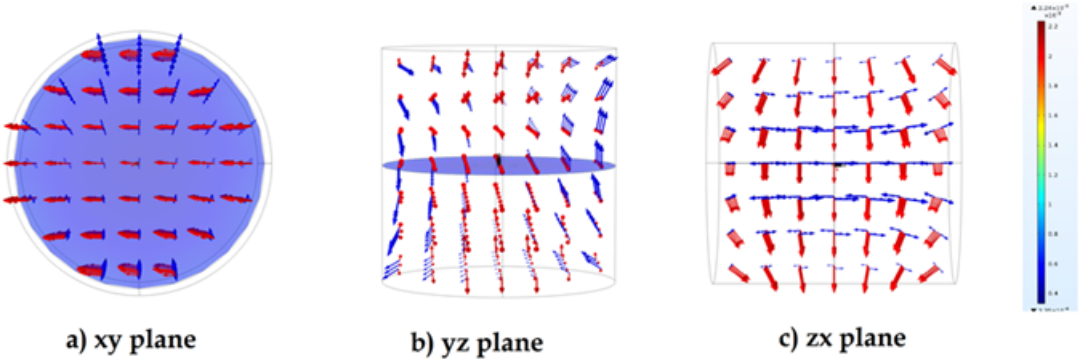

Figure 3.14 Magnetic flux density norm distribution with real (red) and imaginary (blue) part of the magnetic flux density for coil at 63.8 MHz. a) indicates xy plane orientation, b) indicates yz plane orientation, c) indicates zx plane

.

As it is noticed in Figure 3.14, existence of designed RF marker in the low-pass birdcage coil domain didn't cause a significant distortion on both homogeneity and circularity of B_1 field. However main reason for slightly alteration on the magnetic field homogeneity and circularity is RF marker induced additional non–uniform currents on the coil elements due to the different dielectric and permeability properties of the RF marker prototype.

3.4 Electric Fields Norm Analysis of Helical RF Coils in Different Designs

After validation of custom made birdcage coil into MRI environment, orientation depended performance analysis of RF coils were performed into the birdcage coil. For this aim, electric field norms of 2 different RF coils into different orientations according to the birdcage coil were evaluated. Helical coil designs were constructed into virtual platform that have similar geometric size with real RF marker prototypes fabricated in experimental studies.

3.4.1 Electric Fields Norm Analysis of One Helical RF Coil

Electric fields norm of one helical RF coil into different orientations according to the birdcage coil were inspected in order to evaluate orientation dependency of the RF marker with respect to the standard MRI coils.

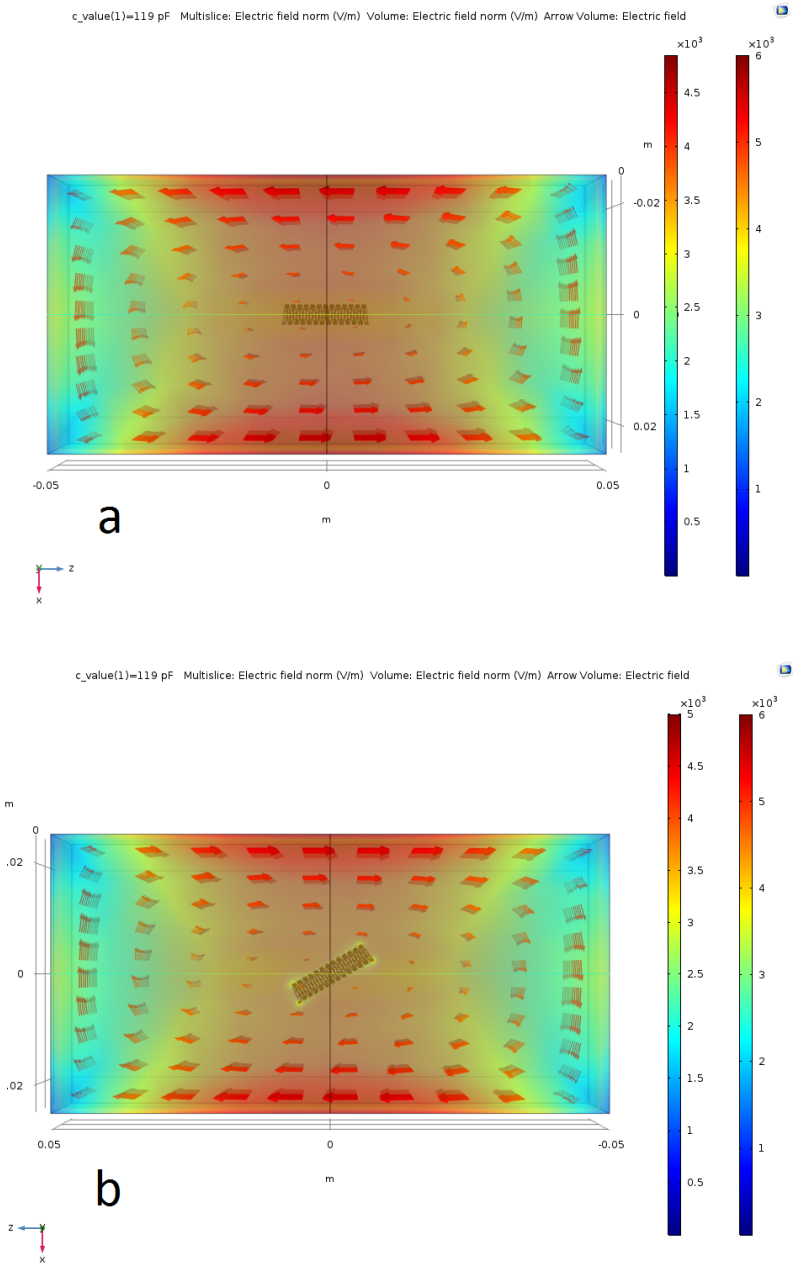

Figure 3.15 Image shows induced electric fields norm into the ASTM phantom and vicinity of the one helical RF coil after the excitation of the birdcage coil at 63.8 MHz. Variation of electric field norms was observed when designed RF coil was a) parallel, and b) 30° rotated according to the birdcage coil. Red arrows show the direction of the electric field into volume of interest.

.

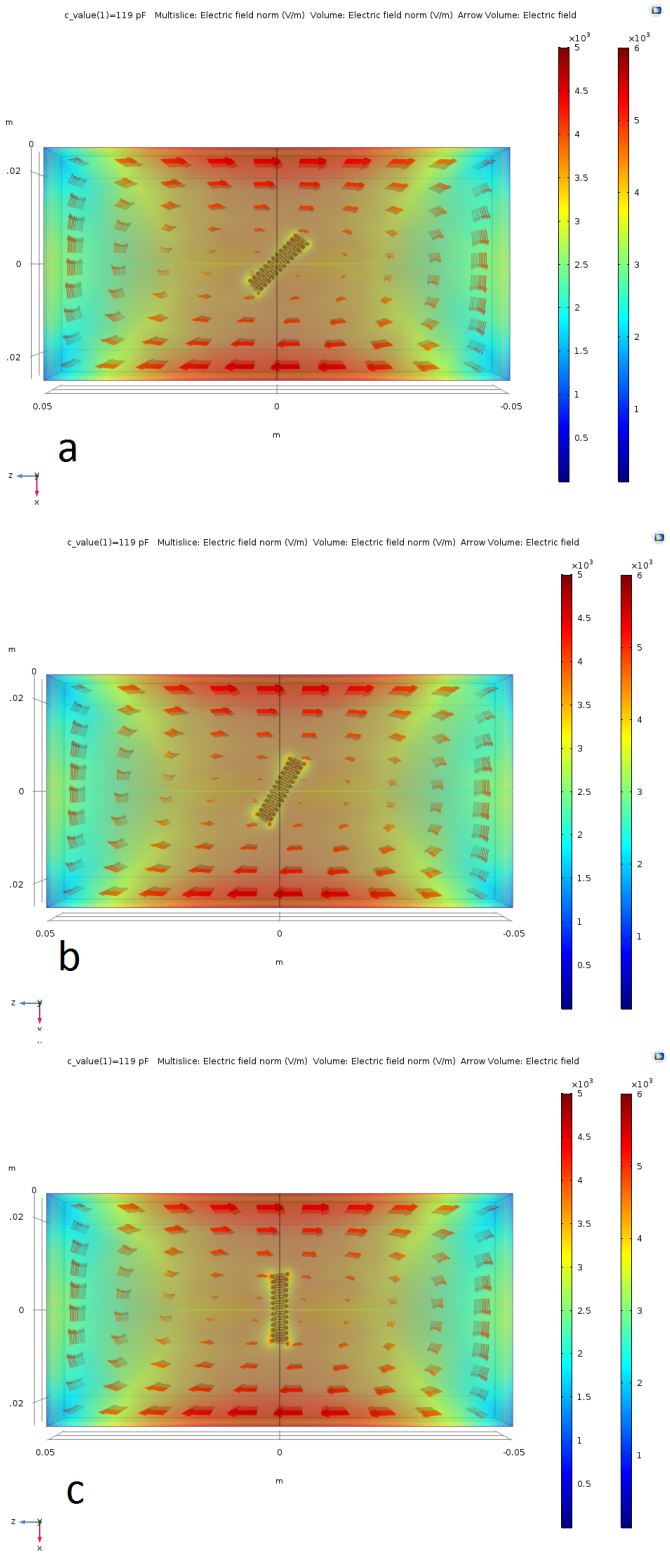

Figure 3.16 Image shows induced electric field norms into the ASTM phantom and vicinity of the designed RF coil after the excitation of the birdcage coil at 63.8 MHz. Variation of electric field norms was observed when designed RF coil was a) 45° rotated, b) 60° rotated, and c) perpendicular according to the birdcage coil. Red arrows show the direction of the electric field into volume of interest.

In Figure 3.15 and Figure 3.16 the amount of electric field varies depending on the orientation of the RF coils. Electric field increases significantly with respect to the increase in rotation angle between the RF coil and the birdcage coil. The highest induced electric field is observed when the RF coil is placed perpendicular to the birdcage coil as it is expected in Maxwell's equations.

Similarly with the excitation by the birdcage coil, electric field norms at the surface of the RF coil were examined in Figure 3.17 . The most induced electric field was seen when the RF coil is oriented perpendicular to the birdcage coil.

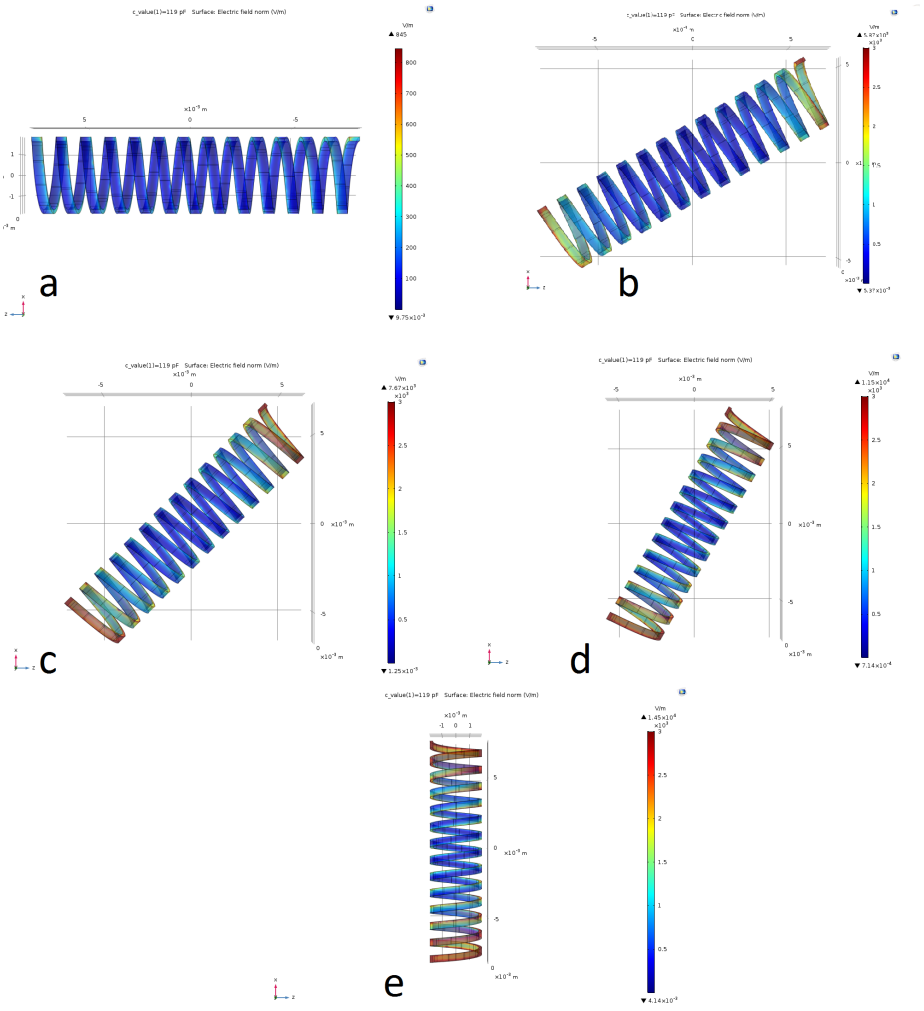

Figure 3.17 Image shows induced electric field norms at the surface of the RF coil after the excitation by the birdcage coil. Electric field norms was observed when the designed RF coil was a) parallel, b) 30° rotated, c) 45° rotated, d) 60° rotated, and e) perpendicular according to the birdcage coil.

.

3.4.2 Electric Field Norm Analysis of Double Helical RF Coil

Another orientation depended performance analysis of RF coil were performed into the birdcage coil by using a different geometric design. Electric fields norm of two helical RF coil into different orientations according to the birdcage coil were observed in order to evaluate orientation dependency of RF markers with respect to the standard MRI coils.

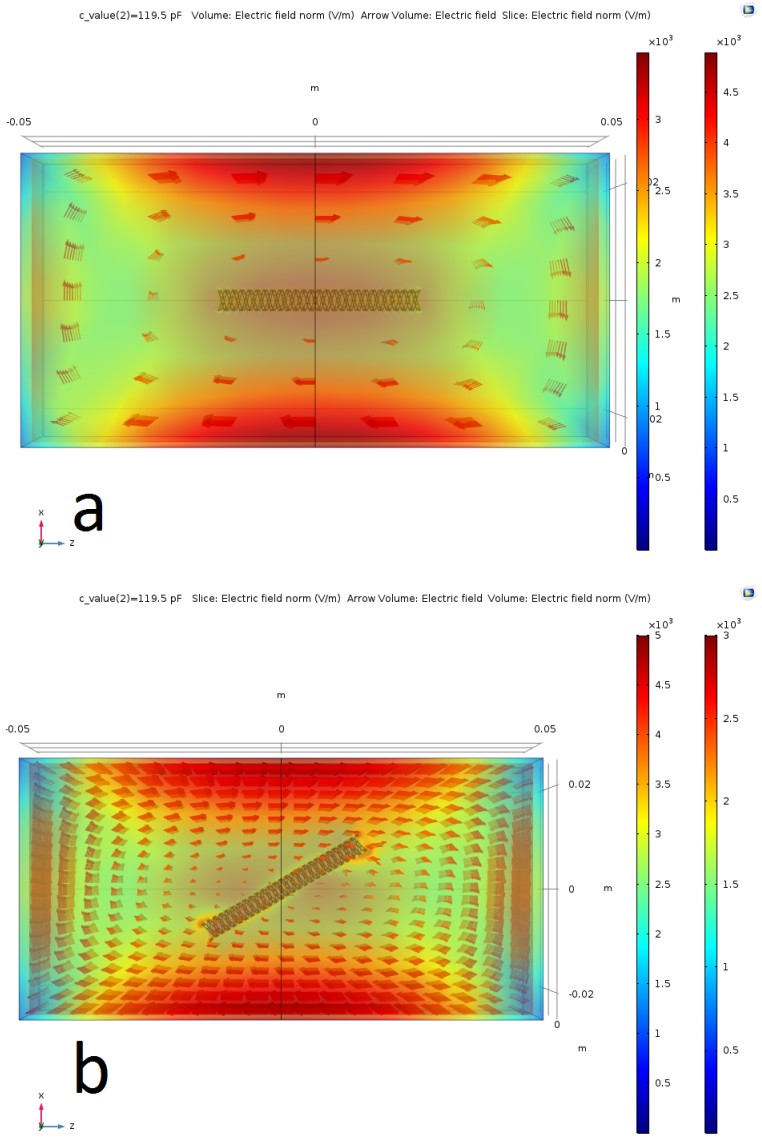

Figure 3.18 Image shows induced electric field norms into the ASTM phantom and vicinity of the designed double RF coil after the exciation of the birdcage coil at 63.8 MHz. Variation of electric field norms was observed when designed double RF coil was a) parallel, and b) 30° rotated according to the birdcage coil. Red arrows show the direction of the electric field into volume of interest.

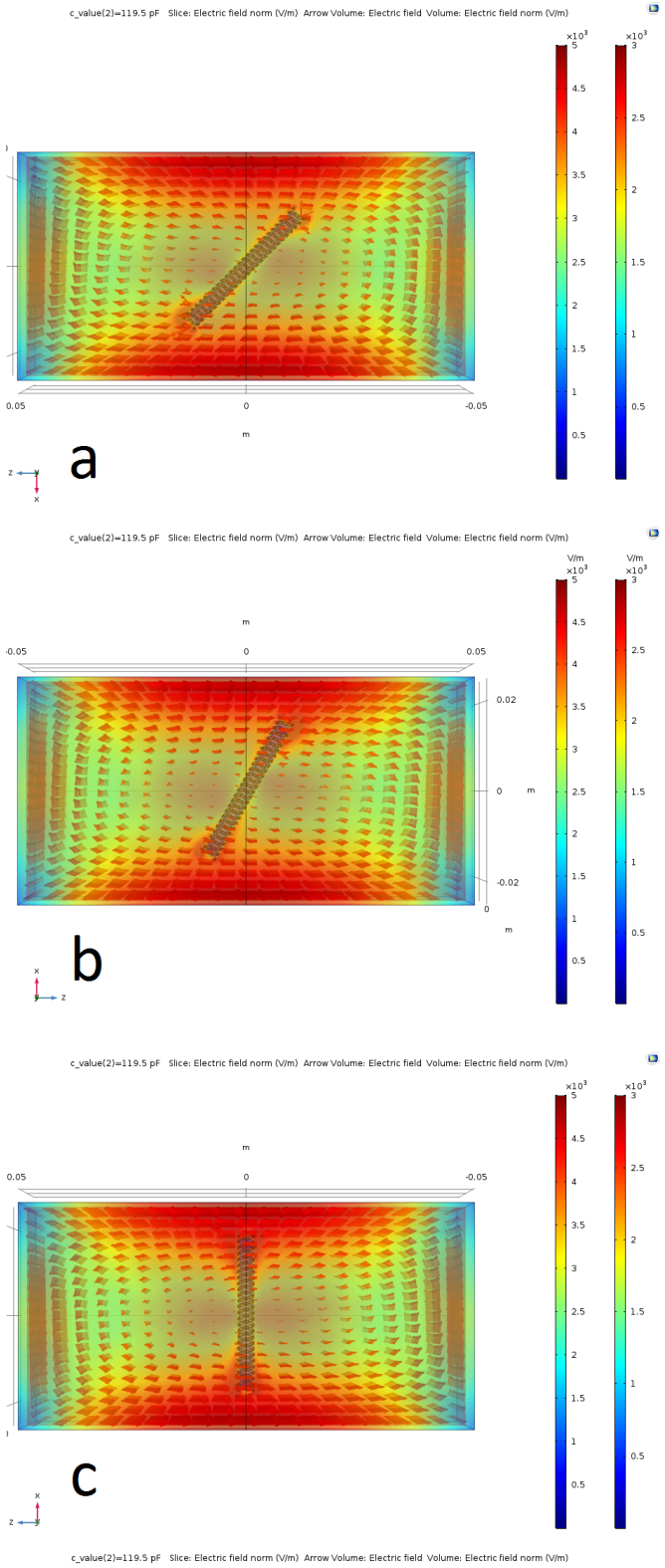

Figure 3.19 Image shows induced electric field norms into the ASTM phantom and vicinity of the designed double RF coil after the excitation of the birdcage coil at 63.8 MHz. Variation of electric field norms was observed when double RF coil was a) 450 rotated, b) 600 rotated, and c) perpendicular according to the birdcage coil. Red arrows show the direction of the electric field into volume of interest.

Similar to one RF coil design, the amount of electric field varies depending on the orientation of the RF coils. Electric field increases significantly with respect to the increase in rotation angle between the double RF coil and the birdcage coil. The highest induced electric field is observed when the double RF coil is placed perpendicular to the birdcage coil as it is expected in Maxwell's equations.

Similarly with the excitation by the birdcage coil, electric field norms at the surface of the double RF coil were examined in Figure 3.20. The most induced electric field was seen when the double RF coil is oriented perpendicular to the birdcage coil.

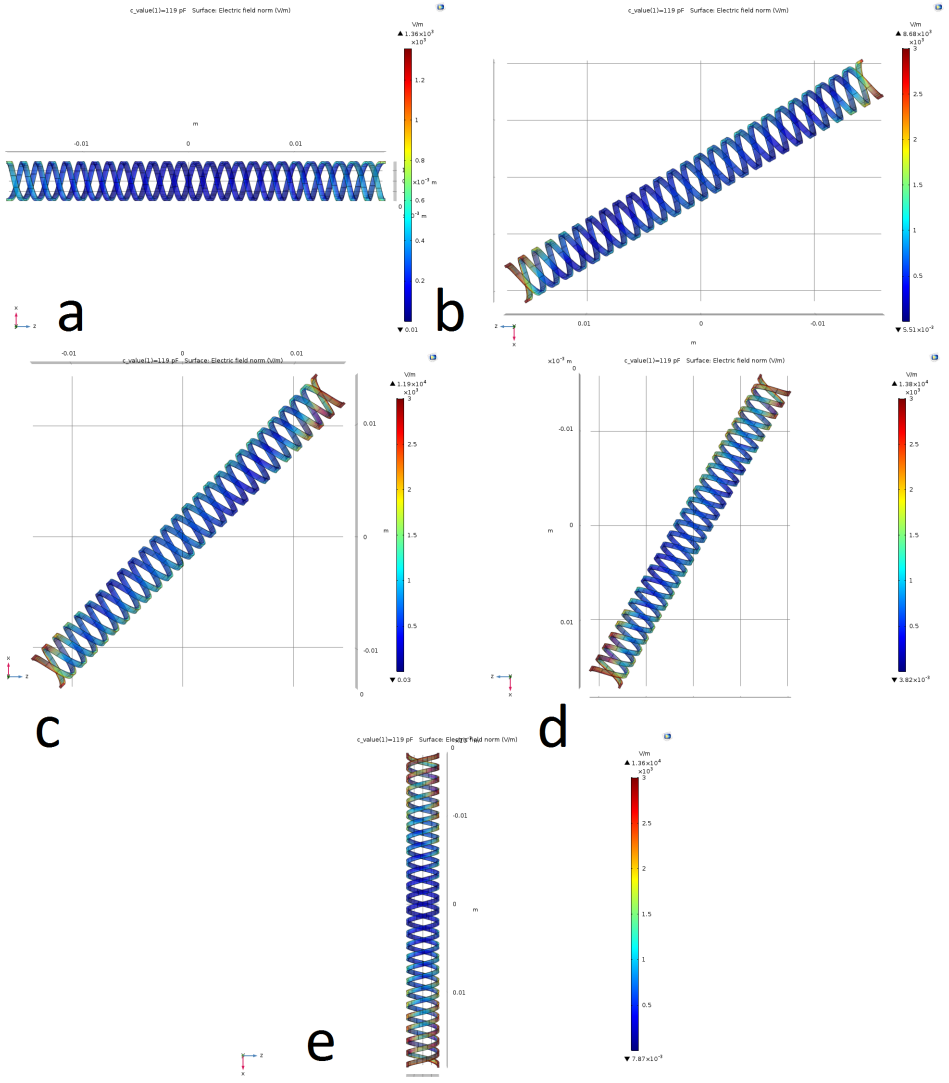

Figure 3.20 Image shows induced electric field norms at the surface of the double RF coil after the excitation by the birdcage coil. Electric fields norm was observed when the designed double RF coil was a) parallel, b) 300 rotated, c) 450 rotated, d) 600 rotated, and e) perpendicular according to the birdcage coil.

In conclusion, the results of simulations are consistent with experimental works and results in the literature. Although there are some difficulties at examining the interactions between micro size instruments and huge size environments such as micro coils and MRI platform, it is clear that the FEM simulations will be a reliable test and evaluation method in order to examine magnetic and electrical characteristics of designed RF coils and so RF markers.

4. DISCUSSION

In this study, a novel microfabrication technique was introduced to form a conspicuous, low profile semi–active RF markers on a non–planar 5 Fr (1.67 mm) catheter surface to highlight the distal device tip under 1.5 T MRI. The MRI safety and MRI visibility tests of manufactured clinical grade semi–active catheter for interventional MRI were realized through in vitro experiments compliance with ASTM standards.

The proposed micro fabrication techniques allow fabricating resonant circuits directly onto the instrument surface and increasing the variety of RF marker designs by using different type of shadow masks during the thermal deposition of metals. It is possible to achieve reliable experimental results that agree with calculations using precise and thin conducting layer masks. Therefore, laser-cut masks from cylindrical structures will enable us to realize unique coil designs such as multi-layer helical coils, tilted coils, double tilted coils, opposed solenoid coil, "Helmholtz" coils, and meander coils. In the future we plan to combine both planar and non–planar RF coil designs (hybrid structures) over the same catheter surface to reach optimal SNR.

By exploiting the methods presented here, it will be possible to manufacture a novel transmission line designs for clinical semi–active or active interventional MRI catheters and guidewires that composed of reversed coil sections wherein the current direction opposes the induced RF field, termed billabong, which is a promising approach to minimize RF induced heating risks under MRI [96].

RF markers mounted into semi–active and active devices comprise excessive size conventional components such as solenoid coils, and non–magnetic capacitors that are not suitable especially for interventional pediatric procedures, due to the risk of injuring blood vessel walls during catheter manipulation within vasculature. Our design implements cylindrical components over the catheter surface, will enable interventional catheters to be steered through tortuous and delicate blood vessels during procedures.

Recently there are some studies [113–115] in measuring the local pressure in blood vessels or regional stiffness that is valuable in the postoperative monitoring of aneurysms or early atherosclerosis. However, except difficulties related with MRI, implanting a conventional pressure sensor equipped with power and a signal cable cause additional risk of infection after the implantation.

After realization of RF markers in our research, it may be possible to implement a pressure sensor by manufacturing a coil and pressure-sensitive capacitor. Since the surrounding pressure has an influence on the capacitance of the designed capacitor and so the magnetic field in close vicinity of the loop coil, the magnetization change of the nearby sample can be observed as a signal variation during MRI. In future, blood leakage can also be detected under MRI, if a small pressure sensor is mounted on the surface of a micro catheter.

In other study of this thesis, 3D FEM modeling of manufactured RF marker prototype into a birdcage coil was figured out by using COMSOL Multiphysics software program. After ensuring the validation of performed MRI platform with compliance with ASTM phantom results, affectivity of the birdcage coil and MRI environment for 1.5 Tesla was examined with capacitance tuning. After obtaining optimum capacitance value, homogeneity of magnetic field was analyzed when the RF marker prototype was placed into center of the birdcage coil. Moreover performances of 2 different RF coil designs were evaluated while coil designs were positioned into different orientation angles with respect to the birdcage coil.

5. CONCLUSION

Currently, there is no commercially available clinical grade, safe and MRI compatible catheters and devices to perform endovascular imaging and treatment under MRI. The manufacturing of a commercial MRI compatible catheter is an extremely complicated task that requires micro size fabrication techniques by considering many factors such as flexibility, endurance, biocompatibility, MRI safety and reproducibility.

Thin film coating technologies expressed hereby can be adapted to the fabrication of varied interventional instruments used in clinic. Additional modifications of the PVD based thin film coating process and electroplating technique will enable new studies to manufacture novel "smart" catheter designs that incorporate various sensors such as temperature, pressure and flow sensors directly on a catheter shaft. Such low profile "smart" catheter devices may enable new clinical approaches and therapeutic applications in cardiovascular MRI such as cardiac pacing (CP), electrophysiology ablation catheters, biopsy needles, and occluders.

Semi–active visualization technology is based on inductive signal coupling between RF markers and standard MRI coils. Since RF markers do not require any electrical (wire) or mechanical (optical fiber) connection between instrument and MR scanner, satisfactory mechanical and imaging characteristics carry semi–active tracking technologies one step further compared to passive and active visualization methods under MRI.

Beside of implementation of RF marker at distal tip of a catheter, the incorporation of multiple RF markers can also provide visualization of even longer segments at overall catheter shaft. Therefore fiducial RF markers that are attractive candidates for whole shaft MRI catheter visibility as well, has enormous potential in future of MRI compatible devices.

Capability of the modeling the interactions between a RF marker and a birdcage coil into a MRI environment that is experienced in this thesis study, will lead many new simulation designs including comparison of different forms of RF markers, coil orientations and their characteristics. Accordingly it is possible to construct custom made novel coil designs that can be used as a RF marker and also as a standard MRI coil.

By providing these simulation models will be very beneficial for saving time to foresee the optimum coil parameters and RF marker performances without fabrication and real MRI experiments.

REFERENCES

1. Kleinerman, R. A., "Cancer risks following diagnostic and therapeutic radiation exposure in children," *Pediatric Radiology*, Vol. 36, no. SUPPL. 14, pp. 121–125, 2006.

2. Andreassi, M. G., L. Ait-Ali, N. Botto, S. Manfredi, G. Mottola, and E. Picano, "Cardiac catheterization and long-term chromosomal damage in children with congenital heart disease," *European Heart Journal*, Vol. 27, no. 22, pp. 2703–2708, 2006.

3. McCullough, P. A., R. Wolyn, L. L. Rocher, R. N. Levin, and W. W. O'Neill, "Acute Renal Failure After Coronary Intervention: Incidence, Risk Factors, and Relationship to Mortality," *The American Journal of Medicine*, Vol. 103, no. 5, pp. 368–375, 1997.

4. UNSCEAR, *Sources and Effects of Ionizing Radiation, United Nations Scientific Committee on the Effects of Atomic Radiation UNSCEAR 2000 Report to the General Assembly, with Scientific Annexes*, Vol. I, 2000.

5. Vano, E., L. Gonzalez, J. M. Fernández, and Z. J. Haskal, "Eye lens exposure to radiation in interventional suites: caution is warranted.," *Radiology*, Vol. 248, no. 3, pp. 945–953, 2008.

6. Goldstein, J. A., S. Balter, M. Cowley, J. Hodgson, and L. W. Klein, "Occupational hazards of interventional cardiologists: Prevalence of orthopedic health problems in contemporary practice," *Catheterization and Cardiovascular Interventions*, Vol. 63, no. 4, pp. 407–411, 2004.

7. Lederman, R. J., "NIH Public Access," Vol. 112, no. 19, pp. 3009–3017, 2006.

8. Barkhausen, J., T. Kahn, G. A. Krombach, C. K. Kuhl, J. Lotz, D. Maintz, J. Ricke, S. O. Schönberg, T. J. Vogl, and F. K. Wacker, "White Paper: Interventional MRI: Current Status and Potential for Development Considering Economic Perspectives, Part 1: General Application," *RoFo : Fortschritte auf dem Gebiete der Rontgenstrahlen und der Nuklearmedizin*, Vol. 189, no. 7, pp. 611–623, 2017.

9. Hussain, T. M, K. Rhode, G. F. Greil, "Interventional Cardiovascular Magnetic Resonance Imaging,'In: Plein S., Greenwood J., Ridgway J. (eds)' *Cardiovascular MR Manual. Springer, Cham*, pp. 463–472, 2015.

10. Muthurangu, V., A. Taylor, R. Andriantsimiavona, S. Hegde, M. E. Miquel, R. Tulloh, E. Baker, D. L. G. Hill, and R. S. Razavi, "Novel method of quantifying pulmonary vascular resistance by use of simultaneous invasive pressure monitoring and phase-contrast magnetic resonance flow," *Circulation*, Vol. 110, no. 7, pp. 826–834, 2004.

11. Mavrogeni, S., and G. Kolovou, "Role of cardiovascular magnetic resonance in interventional cardiology," *Continuing Cardiology Education*, Vol. 2, no. 1, pp. 25–31, 2016.

12. Raman, V. K., P. V. Karmarkar, M. A. Guttman, A. J. Dick, D. C. Peters, C. Ozturk, B. S. Pessanha, R. B. Thompson, A. N. Raval, R. DeSilva, R. J. Aviles, E. Atalar, E. R. McVeigh, and R. J. Lederman, "Real-time magnetic resonance-guided endovascular repair of experimental abdominal aortic aneurysm in swine," *Journal of the American College of Cardiology*, Vol. 45, no. 12, pp. 2069–2077, 2005.

13. Eggebrecht, H., H. Kühl, G. M. Kaiser, S. Aker, M. O. Zenge, F. Stock, F. Breuckmann, F. Grabellus, M. E. Ladd, R. H. Mehta, R. Erbel, and H. H. Quick, "Feasibility of real-time magnetic resonance-guided stent-graft placement in a swine model of descending aortic dissection," *European Heart Journal*, Vol. 27, no. 5, pp. 613–620, 2006.

14. Raval, A. N., J. D. Telep, M. A. Guttman, C. Ozturk, M. Jones, R. B. Thompson, V. J. Wright, W. H. Schenke, R. DeSilva, R. J. Aviles, V. K. Raman, M. C. Slack, and R. J. Lederman, "Real-time magnetic resonance imaging-guided stenting of aortic coarctation with commercially available catheter devices in swine," *Circulation*, Vol. 112, no. 5, pp. 699–706, 2005.

15. Buecker, A., E. Spuentrup, R. Grabitz, F. Freudenthal, E. G. Muehler, T. Schaeffter, J. J. van Vaals, and R. W. Gunther, "Magnetic resonance-guided placement of atrial septal closure device in animal model of patent foramen ovale," *Circulation*, Vol. 106, no. 4, pp. 511–515, 2002.

16. Rickers, C., M. Jerosch-Herold, X. Hu, N. Murthy, X. Wang, H. Kong, R. T. Seethamraju, J. Weil, and N. M. Wilke, "Magnetic resonance image-guided transcatheter closure of atrial septal defects," *Circulation*, Vol. 107, no. 1, pp. 132–138, 2003.

17. Schalla, S., M. Saeed, C. B. Higgins, O. Weber, A. Martin, and P. Moore, "Balloon sizing and transcatheter closure of acute atrial septal defects guided by magnetic resonance fluoroscopy: Assessment and validation in a large animal model," *Journal of Magnetic Resonance Imaging*, Vol. 21, no. 3, pp. 204–211, 2005.

18. Raval, A. N., P. V. Karmarkar, M. A. Guttman, C. Ozturk, S. Sampath, R. DeSilva, R. J. Aviles, M. Xu, V. J. Wright, W. H. Schenke, O. Kocaturk, A. J. Dick, V. K. Raman, E. Atalar, E. R. McVeigh, and R. J. Lederman, "Real-time magnetic resonance imaging-guided endovascular recanalization of chronic total arterial occlusion in a swine model," *Circulation*, Vol. 113, no. 8, pp. 1101–1107, 2006.

19. Krombach, G. a., J. G. Pfeffer, S. Kinzel, M. Katoh, R. W. Günther, and A. Buecker, "MR-guided percutaneous intramyocardial injection with an MR-compatible catheter: feasibility and changes in T1 values after injection of extracellular contrast medium in pigs.," *Radiology*, Vol. 235, no. 2, pp. 487–94, 2005.

20. Frahm, C., H. B. Gehl, H. Lorch, M. Zwaan, M. Drobnitzky, G. A. Laub, and H. D. Weiss, "MR-guided placement of a temporary vena cava filter: Technique and feasibility," *Journal of Magnetic Resonance Imaging*, Vol. 8, no. 1, pp. 105–109, 1998.

21. Bartels, L. W., C. Bos, R. D. Van Weide, H. F. M. Smits, C. J. G. Bakker, and M. A. Viergever, "Placement of an inferior vena cava filter in a pig guided by high-resolution MR fluoroscopy at 1.5 T," *Journal of Magnetic Resonance Imaging*, Vol. 12, no. 4, pp. 599–605, 2000.

22. Bücker, A., J. M. Neuerburg, G. B. Adam, A. Glowinski, T. Schaeffter, V. Rasche, J. J. Van Vaals, and R. W. Günther, "Real-time MR guidance for inferior vena cava filter placement in an animal model," *Journal of Vascular and Interventional Radiology*, Vol. 12, no. 6, pp. 753–756, 2001.

23. Shih, M. C. P., W. J. Rogers, H. Bonatti, and K. D. Hagspiel, "Real-time MR-guided retrieval of inferior vena cava filters: An in vitro and animal model study," *Journal of Vascular and Interventional Radiology*, Vol. 22, no. 6, pp. 843–850, 2011.

24. Lardo, A. C., E. R. McVeigh, P. Jumrussirikul, R. D. Berger, H. Calkins, J. Lima, and H. R. Halperin, "Visualization and temporal/spatial characterization of cardiac radiofrequency ablation lesions using magnetic resonance imaging," *Circulation*, Vol. 102, no. 6, pp. 698–705, 2000.

25. Kolandaivelu, A., M. M. Zviman, V. Castro, A. C. Lardo, R. D. Berger, and H. R. Halperin, "Noninvasive assessment of tissue heating during cardiac radiofrequency ablation using MRI thermography," *Circulation: Arrhythmia and Electrophysiology*, Vol. 3, no. 5, pp. 521–529, 2010.

26. Baysoy, E., D. Yildirim, C. Ozsoy, S. Mutlu, and O. Kocaturk, "Erratum to: Thin film based semi-active resonant marker design for low profile interventional cardiovascular MRI devices (Magnetic Resonance Materials in Physics, Biology and Medicine, (2017), 30, 1, (93-101), 10.1007/s10334-016-0586-8)," *Magnetic Resonance Materials in Physics, Biology and Medicine*, Vol. 30, no. 1, 2016.

27. Zijlstra, F., *Knowledge-based acceleration of MRI for metal object localization*, 1985.

28. Seppenwoolde, J. H., M. A. Viergever, and C. J. Bakker, "Passive tracking exploiting local signal conservation: The white marker phenomenon," *Magnetic Resonance in Medicine*, Vol. 50, no. 4, pp. 784–790, 2003.

29. Kozerke, S., and J. Tsao, "Reduced data acquisition methods in cardiac imaging," 2004.

30. Magnusson, P., E. Johansson, S. Månsson, J. S. Petersson, C. M. Chai, G. Hansson, O. Axelsson, and K. Golman, "Passive catheter tracking during interventional MRI using hyperpolarized13C," *Magnetic Resonance in Medicine*, Vol. 57, no. 6, pp. 1140–1147, 2007.

31. Bakker, C. J., R. M. Hoogeveen, J. Weber, J. J. Van Vaals, M. A. Viergever, and W. P. Mali, "Visualization of dedicated catheters using fast scanning techniques with potential for MR-guided vascular interventions," *Magnetic Resonance in Medicine*, Vol. 36, no. 6, pp. 816–820, 1996.

32. Nanz, D., D. Weishaupt, H. H. Quick, and J. F. Debatin, "TE-switched double-contrast enhanced visualization of vascular system and instruments for MR-guided interventions," *Magnetic Resonance in Medicine*, Vol. 43, no. 5, pp. 645–648, 2000.

33. Prince, M. R., "Gadolinium-enhanced MR aortography.," *Radiology*, Vol. 191, no. 1, pp. 155–164, 1994.

34. Omary, R. A., O. Unal, D. S. Koscielski, R. Frayne, F. R. Korosec, C. A. Mistretta, C. M. Strother, and T. M. Grist, "Real-time MR imaging-guided passive catheter tracking with use of gadolinium-filled catheters," *Journal of Vascular and Interventional Radiology*, Vol. 11, no. 8, pp. 1079–1085, 2000.

35. Bakker, C. J. G., C. Bos, and H. J. Weinmann, "Passive tracking of catheters and guidewires by contrast-enhanced MR fluoroscopy," *Magnetic Resonance in Medicine*, Vol. 45, no. 1, pp. 17–23, 2001.

36. Draper, J. N., M. L. Lauzon, and R. Frayne, "Passive catheter visualization in magnetic resonance-guided endovascular therapy using multicycle projection dephasers," *Journal of Magnetic Resonance Imaging*, Vol. 24, no. 1, pp. 160–167, 2006.

37. Dominguez-Viqueira, W., H. Karimi, W. W. Lam, and C. H. Cunningham, "A controllable susceptibility marker for passive device tracking," *Magnetic Resonance in Medicine*, Vol. 72, no. 1, pp. 269–275, 2014.

38. Rubin, D. A., and J. B. Kneeland, "MR imaging of the musculoskeletal system: technical considerations for enhancing image quality and diagnostic yield.," *AJR. American journal of roentgenology*, Vol. 163, no. 5, pp. 1155–63, 1994.

39. Frericks, B. B., D. R. Elgort, C. Hillenbrand, J. L. Duerk, J. S. Lewin, and F. K. Wacker, "Magnetic resonance imaging-guided renal artery stent placement in a Swine model: comparison of two tracking techniques.," *Acta radiologica (Stockholm, Sweden : 1987)*, Vol. 50, no. 1, pp. 21–7, 2009.

40. Settecase, F., A. J. Martin, P. Lillaney, A. Losey, and S. W. Hetts, "Magnetic Resonance-Guided Passive Catheter Tracking for Endovascular Therapy," 2015.

41. Lederman, R. J., "Cardiovascular interventional magnetic resonance imaging," *Circulation*, Vol. 112, no. 19, pp. 3009–3017, 2005.

42. Patil, S., "Passive tracking and system interfaces for interventional MRI," 2009.

43. Griffin, G. H., K. J. Anderson, H. Celik, and G. A. Wright, "Safely assessing radiofrequency heating potential of conductive devices using image-based current measurements," *Magnetic Resonance in Medicine*, Vol. 73, no. 1, pp. 427–441, 2015.

44. Zimmermann-Paul, G. G., M. E. Ladd, T. Pfammatter, P. R. Hilfiker, H. H. Quick, and J. F. Debatin, "MR versus fluoroscopic guidance of a catheter/guidewire system: In vitro comparison of steerability," *Journal of Magnetic Resonance Imaging*, Vol. 8, no. 5, pp. 1177–1181, 1998.

45. Kantor, H. L., R. W. Briggs, and R. S. Balaban, "In vivo 31P nuclear magnetic resonance measurements in canine heart using a catheter-coil.," *Circulation research*, Vol. 55, no. 2, pp. 261–6, 1984.

46. Glowinski, A., G. Adam, A. Bücker, J. Neuerburg, J. J. Van Vaals, and R. W. Günther, "Catheter visualization using locally induced, actively controlled field inhomogeneities," *Magnetic Resonance in Medicine*, Vol. 38, no. 2, pp. 253–258, 1997.

47. Ocali, O., and E. Atalar, "Intravascular magnetic resonance imaging using a loopless catheter antenna," *Magnetic Resonance in Medicine*, Vol. 37, no. 1, pp. 112–118, 1997.

48. Susil, R. C., C. J. Yeung, and E. Atalar, "Intravascular extended sensitivity (IVES) MRI antennas," *Magnetic Resonance in Medicine*, Vol. 50, no. 2, pp. 383–390, 2003.

49. Karmarkar, P. V., D. L. Kraitchman, I. Izbudak, L. V. Hofmann, L. C. Amado, D. Fritzges, R. Young, M. Pittenger, J. W. M. Bulte, and E. Atalar, "MR-trackable intramyocardial injection catheter," *Magnetic Resonance in Medicine*, Vol. 51, no. 6, pp. 1163–1172, 2004.

50. Tsekos, N. V., E. Atalar, D. Li, R. A. Omary, J. M. Serfaty, and P. K. Woodard, "Magnetic resonance imaging-guided coronary interventions," *Journal of Magnetic Resonance Imaging*, Vol. 19, no. 6, pp. 734–749, 2004.

51. Arepally, A., P. V. Karmarkar, C. Weiss, E. R. Rodriguez, R. J. Lederman, and E. Atalar, "Magnetic resonance image-guided trans-septal puncture in a swine heart," *Journal of Magnetic Resonance Imaging*, Vol. 21, no. 4, pp. 463–467, 2005.

52. Sathyanarayana, S., P. Aksit, A. Arepally, P. V. Karmarkar, M. Solaiyappan, and E. Atalar, "Tracking planar orientations of active MRI needles," *Journal of Magnetic Resonance Imaging*, Vol. 26, no. 2, pp. 386–391, 2007.

53. Bell, J. A., C. E. Saikus, K. Ratnayaka, V. Wu, M. Sonmez, A. Z. Faranesh, J. H. Colyer, R. J. Lederman, and O. Kocaturk, "A deflectable guiding catheter for real-time MRI-guided interventions," *Journal of Magnetic Resonance Imaging*, Vol. 35, no. 4, pp. 908–915, 2012.

54. Kocaturk, O., C. E. Saikus, M. A. Guttman, A. Z. Faranesh, K. Ratnayaka, C. Ozturk, E. R. McVeigh, and R. J. Lederman, "Whole shaft visibility and mechanical performance for active MR catheters using copper-nitinol braided polymer tubes," *Journal of Cardiovascular Magnetic Resonance*, Vol. 11, no. 1, pp. 1–10, 2009.

55. Zuehlsdorff, S., R. Umathum, S. Volz, P. Hallscheidt, C. Fink, W. Semmler, and M. Bock, "MR coil design for simultaneous tip tracking and curvature delineation of a catheter," *Magnetic Resonance in Medicine*, Vol. 52, no. 1, pp. 214–218, 2004.

56. Krahn, P. R., S. M. Singh, V. Ramanan, L. Biswas, N. Yak, K. J. Anderson, J. Barry, M. Pop, and G. A. Wright, "Cardiovascular magnetic resonance guided ablation and intra-procedural visualization of evolving radiofrequency lesions in the left ventricle," *Journal of Cardiovascular Magnetic Resonance*, Vol. 20, no. 1, pp. 1–12, 2018.

57. Atalar, E., P. A. Bottomley, O. Ocali, L. C. Correia, M. D. Kelemen, J. A. Lima, and E. A. Zerhouni, "High resolution intravascular MRI and MRS by using a catheter receiver coil," *Magnetic Resonance in Medicine*, Vol. 36, no. 4, pp. 596–605, 1996.

58. Fandrey, S., S. Weiss, and J. Müller, "A novel active MR probe using a miniaturized optical link for a 1.5-T MRI scanner," *Magnetic Resonance in Medicine*, Vol. 67, no. 1, pp. 148–155, 2012.

59. Kuehne, T., R. Fahrig, and K. Butts, "Pair of resonant fiducial markers for localization of endovascular catheters at all catheter orientations," *Journal of Magnetic Resonance Imaging*, Vol. 17, no. 5, pp. 620–624, 2003.

60. Zhang, Q., M. Wendt, A. J. Aschoff, J. S. Lewin, and J. L. Duerk, "A multielement RF coil for MRI guidance of interventional devices," *Journal of Magnetic Resonance Imaging*, Vol. 14, no. 1, pp. 56–62, 2001.

61. Quick, H. H., M. O. Zenge, H. Kuehl, G. M. Kaiser, S. Aker, H. Eggebrecht, S. Massing, and M. E. Ladd, "Wireless Active Catheter Visualization : Passive Decoupling Methods and Their Impact on Catheter Visibility," *Ismrm*, Vol. 13, no. c, p. 2164, 2005.

62. Versluis, M. J., N. Tsekos, N. B. Smith, and A. G. Webb, "Simple RF design for human functional and morphological cardiac imaging at 7 tesla," *Journal of Magnetic Resonance*, Vol. 200, no. 1, pp. 161–166, 2009.

63. Kaiser, M., M. Detert, M. A. Rube, A. El-Tahir, O. J. Elle, A. Melzer, B. Schmidt, and G. H. Rose, "Resonant marker design and fabrication techniques for device visualization during interventional magnetic resonance imaging," *Biomedizinische Technik*, Vol. 60, no. 2, pp. 89–103, 2015.

64. Alipour, A., S. Gokyar, O. Algin, E. Atalar, and H. V. Demir, "An inductively coupled ultra-thin, flexible, and passive RF resonator for MRI marking and guiding purposes: Clinical feasibility," *Magnetic Resonance in Medicine*, Vol. 80, no. 1, pp. 361–370, 2018.

65. Demas, V., A. Bernhardt, V. Malba, K. L. Adams, L. Evans, C. Harvey, R. S. Maxwell, and J. L. Herberg, "Electronic characterization of lithographically patterned microcoils for high sensitivity NMR detection," *Journal of Magnetic Resonance*, Vol. 200, no. 1, pp. 56–63, 2009.

66. Picard, Y. N., D. P. Adams, M. J. Vasile, and M. B. Ritchey, "Focused ion beam-shaped microtools for ultra-precision machining of cylindrical components," *Precision Engineering*, Vol. 27, no. 1, pp. 59–69, 2003.

67. Sillerud, L. O., A. F. McDowell, N. L. Adolphi, R. E. Serda, D. P. Adams, M. J. Vasile, and T. M. Alam, "1H NMR Detection of superparamagnetic nanoparticles at 1 T using a microcoil and novel tuning circuit," *Journal of Magnetic Resonance*, Vol. 181, no. 2, pp. 181–190, 2006.

68. Kong, T. F., W. K. Peng, T. D. Luong, N.-T. Nguyen, and J. Han, "Adhesive-based liquid metal radio-frequency microcoil for magnetic resonance relaxometry measurement," *Lab Chip*, Vol. 12, no. 2, pp. 287–294, 2012.

69. Rogers, J. A., R. J. Jackman, G. M. Whitesides, D. L. Olson, and J. V. Sweedler, "Using microcontact printing to fabricate microcoils on capillaries for high resolution proton nuclear magnetic resonance on nanoliter volumes," *Applied Physics Letters*, Vol. 70, no. 18, pp. 2464–2466, 1997.

70. Fandrey, S., S. Weiss, and J. Müller, "A Novel Intravascular MRI Coil with optimized Sensitivity," *Proceedings 16th Scientific Meeting, International Society for Magnetic Resonance in Medicine*, Vol. Toronto, no. 4, p. 1209, 2008.

71. Golda, D., J. H. Lang, and M. L. Culpepper, "Two-layer electroplated microcoils with a PECVD silicon dioxide interlayer dielectric," *Journal of Microelectromechanical Systems*, Vol. 17, no. 6, pp. 1537–1545, 2008.

72. Weiss, S., P. Vernickel, T. Schaeffter, V. Schulz, and B. Gleich, "Transmission line for improved RF safety of interventional devices," *Magnetic Resonance in Medicine*, Vol. 54, no. 1, pp. 182–189, 2005.

73. Nguyen, N. T., K. M. Ng, and X. Huang, "Manipulation of ferrofluid droplets using planar coils," *Applied Physics Letters*, Vol. 89, no. 5, 2006.

74. Beyzavi, A., and N. T. Nguyen, "Modeling and optimization of planar microcoils," *Journal of Micromechanics and Microengineering*, Vol. 18, no. 9, 2008.

75. Stocker, J. E., A. G. Webb, T. L. Peck, M. Feng, and R. L. Magin, "Nanoliter volume, high-resolution NMR microspectroscopy using a 60-/m planar microcoil," *IEEE Transactions on Biomedical Engineering*, Vol. 44, no. 11, pp. 1122–1127, 1997.

76. Massin, C., G. Boero, F. Vincent, J. Abenhaim, P. A. Besse, and R. S. Popovic, "High-Q factor RF planar microcoils for micro-scale NMR spectroscopy," in *Sensors and Actuators, A: Physical*, Vol. 97-98, pp. 280–288, 2002.

77. Walton, J. H., J. S. De Ropp, M. V. Shutov, A. G. Goloshevsky, M. J. McCarthy, R. L. Smith, and S. D. Collinst, "A micromachined double-tuned NMR microprobe," *Analytical Chemistry*, Vol. 75, no. 19, pp. 5030–5036, 2003.

78. Blaimer, M., F. Breuer, M. Mueller, R. M. Heidemann, M. A. Griswold, and P. M. Jakob, "SMASH, SENSE, PILS, GRAPPA. How to Choose the Optimal Method," 2004.

79. Goloshevsky, A. G., J. H. Walton, M. V. Shutov, J. S. De Ropp, S. D. Collins, and M. J. McCarthy, "Development of low field nuclear magnetic resonance microcoils," *Review of Scientific Instruments*, Vol. 76, no. 2, 2005.

80. Woytasik, M., J. P. Grandchamp, E. Dufour-Gergam, J. P. Gilles, S. Megherbi, E. Martincic, H. Mathias, and P. Crozat, "Two- and three-dimensional microcoil fabrication process for three-axis magnetic sensors on flexible substrates," *Sensors and Actuators, A: Physical*, Vol. 132, no. 1 SPEC. ISS., pp. 2–7, 2006.

81. Jackson, D. D., C. Aracne-Ruddle, V. Malba, S. T. Weir, S. A. Catledge, and Y. K. Vohra, "Magnetic susceptibility measurements at high pressure using designer diamond anvils," *Review of Scientific Instruments*, Vol. 74, no. 4, pp. 2467–2471, 2003.

82. Malba, V., R. Maxwell, L. B. Evans, A. F. Bernhardt, M. Cosman, and K. Yan, "Laser-Lathe Lithography - A Novel Method for Manufacturing Nuclear Magnetic Resonance Microcoils," *Biomedical Microdevices*, Vol. 5, no. 1, pp. 21–27, 2003.

83. Jackman, R. J., J. L. Wilbur, and G. M. Whitesides, "Fabrication of submicrometer features on curved substrates by microcontact printing," *Science*, Vol. 269, no. 5224, pp. 664–666, 1995.

84. Jacobsen, S., D. Wells, C. Davis, and J. Wood, "Fabrication of micro-structures using non-planar lithography (NPL)," *[1991] Proceedings. IEEE Micro Electro Mechanical Systems*, pp. 45–50, 1991.

85. Joshima, Y., T. Kokubo, and T. Horiuchi, "Application of laser scan lithography to fabrication of microcylindrical parts," in *Japanese Journal of Applied Physics, Part 1: Regular Papers and Short Notes and Review Papers*, Vol. 43, pp. 4031–4035, 2004.

86. Goto, S., T. Matsunaga, Y. Matsuoka, K. Kuroda, M. Esashi, and Y. Haga, "Development of high-resolution intraluminal and intravascular MRI probe using microfabrication on cylindrical substrates," *2007 IEEE 20th International Conference on Micro Electro Mechanical Systems (MEMS)*, Vol. 0, no. January, pp. 329–332, 2007.

87. M. Blaimer', T.E. Lanz', M. Griswoldl, F. Fidler', A. H., and A. Webb', "An Inductively Coupled Dipole Resonator for Interventional Applications," Vol. 10, p. 2002, 2002.

88. Ahmad, M. M., R. R. Syms, I. R. Young, B. Mathew, W. Casperz, S. D. Taylor-Robinson, C. A. Wadsworth, and W. M. Gedroyc, "Catheter-based flexible microcoil RF detectors for internal magnetic resonance imaging," *Journal of Micromechanics and Microengineering*, Vol. 19, no. 7, 2009.

89. Watzlaw, J., S. Glöggler, B. Blümich, W. Mokwa, and U. Schnakenberg, "Stacked planar micro coils for single-sided NMR applications," *Journal of Magnetic Resonance*, Vol. 230, pp. 176–185, 2013.

90. Ellersiek, D., H. Fassbender, P. Bruners, J. G. Pfeffer, T. Penzkofer, A. H. Mahnken, T. Schmitz-Rode, W. Mokwa, and U. Schnakenberg, "A monolithically fabricated flexible resonant circuit for catheter tracking in magnetic resonance imaging," *Sensors and Actuators, B: Chemical*, Vol. 144, no. 2, pp. 432–436, 2010.

91. ICNIRP, "ICNIRP Guidelines for limiting exposure to time varying electric, magnetic and electromagnetic fields (up to 300 GHz)," *ICNIRP Publication*, Vol. 74, no. 4, pp. 494–523, 1998.

92. Atalar, E., "Safe Coaxial Cables," *Proceedings of the 7th Annual Meeting of ISMRM, Philadelphia.*, no. c, p. 1006, 1999.

93. Atalar, E., D. L. Kraitchman, B. Carkhuff, J. Lesho, O. Ocali, M. Solaiyappan, M. A. Guttman, and H. K. Charles, "Catheter-tracking FOV MR fluoroscopy," *Magnetic Resonance in Medicine*, Vol. 40, no. 6, pp. 865–872, 1998.

94. Ladd, M. E., H. H. Quick, and J. F. Debatin, "Interventional MRA and intravascular imaging," 2000.

95. Vernickel, P., V. Schulz, S. Weiss, and B. Gleich, "A safe transmission line for MRI," *IEEE Transactions on Biomedical Engineering*, 2005.

96. Bottomley, "Towards MRI-safe implanted leads: a comparative evaluation of four designs," Vol. 18, p. 1101, 2010.

97. Saikus, C. E., and R. J. Lederman, "Interventional Cardiovascular Magnetic Resonance Imaging. A New Opportunity for Image-Guided Interventions," *JACC: Cardiovascular Imaging*, Vol. 2, no. 11, pp. 1321–1331, 2009.

98. Gutiérrez, L. F., R. De Silva, C. Ozturk, M. Sonmez, A. M. Stine, A. N. Raval, V. K. Raman, V. Sachdev, R. J. Aviles, M. A. Waclawiw, E. R. McVeigh, and R. J. Lederman, "Technology preview: X-ray fused with magnetic resonance during invasive cardiovascular procedures," *Catheterization and Cardiovascular Interventions*, Vol. 70, no. 6, pp. 773–782, 2007.

99. De Silva, R., L. F. Gutiérrez, A. N. Raval, E. R. McVeigh, C. Ozturk, and R. J. Lederman, "X-ray fused with magnetic resonance imaging (XFM) to target endomyocardial injections: Validation in a swine model of myocardial infarction," *Circulation*, Vol. 114, no. 22, pp. 2342–2350, 2006.

100. Ratnayaka, K., V. K. Raman, A. Z. Faranesh, M. Sonmez, J. H. Kim, L. F. Gutiérrez, C. Ozturk, E. R. McVeigh, M. C. Slack, and R. J. Lederman, "Antegrade Percutaneous Closure of Membranous Ventricular Septal Defect Using X-Ray Fused With Magnetic Resonance Imaging," *JACC: Cardiovascular Interventions*, Vol. 2, no. 3, pp. 224–230, 2009.

101. Dickfeld, T., H. Calkins, M. Zviman, R. Kato, G. Meininger, L. Lickfett, R. Berger, H. Halperin, and S. B. Solomon, "Anatomic Stereotactic Catheter Ablation on Three-Dimensional Magnetic Resonance Images in Real Time," *Circulation*, Vol. 108, no. 19, pp. 2407–2413, 2003.

102. Edelstein, W. A., G. H. Glover, C. J. Hardy, and R. W. Redington, "The intrinsic signal-to-noise ratio in NMR imaging," *Magnetic Resonance in Medicine*, Vol. 3, no. 4, pp. 604–618, 1986.

103. Hoult, D. I., and R. E. Richards, "The Signal-to-Noise Ratio of the Nuclear Magnetic Resonance Experiment ! P rms = KrlMo (PO Quo Vc / JFkTJf Y," *Ratio*, Vol. 85, pp. 71–85, 1976.

104. Hoult, D. I., "The NMR receiver: A description and analysis of design," 1978.

105. Minard, K. R., and R. A. Wind, "Solenoidal microcoil design - Part II: Optimizing winding parameters for maximum signal-to-noise performance," *Concepts in Magnetic Resonance*, Vol. 13, no. 3, pp. 190–210, 2001.

106. Minard, K. R., and R. A. Wind, "Solenoidal microcoil design. Part I: Optimizing RF homogeneity and coil dimensions," *Concepts in Magnetic Resonance*, Vol. 13, no. 2, pp. 128–142, 2001.

107. Quick, H. H., H. Kuehl, G. Kaiser, S. Bosk, J. F. Debatin, and M. E. Ladd, "Inductively coupled stent antennas in MRI," *Magnetic Resonance in Medicine*, Vol. 48, no. 5, pp. 781–790, 2002.

108. Lou, H. H., and Y. Huang, "Electroplating," *Encyclopedia of Chemical Processing*, pp. 1–10, 2006.

109. Gurler, N., and Y. Z. Ider, "Numerical methods and software tools for simulation, design, and resonant mode analysis of radio frequency birdcage coils used in MRI," *Concepts in Magnetic Resonance Part B: Magnetic Resonance Engineering*, Vol. 45, no. 1, pp. 13–32, 2015.

110. Tadesse, Y.,"The electromagnetic simulation of birdcage coils for MRI based on finite element method," Master of degree thesis, Youngstown State University, Ohio, The United States of America, 2015.

111. Sonmez, M., C. E. Saikus, J. A. Bell, D. N. Franson, M. Halabi, A. Z. Faranesh, C. Ozturk, R. J. Lederman, and O. Kocaturk, "MRI active guidewire with an embedded temperature probe and providing a distinct tip signal to enhance clinical safety," *Journal of Cardiovascular Magnetic Resonance*, Vol. 14, no. 1, 2012.

112. Collins, C. M., and Z. Wang, "NIH Public Access," Vol. 65, no. 5, pp. 1470–1482, 2012.

113. Myllylä, T. S., A. A. Elseoud, H. S. S. Sorvoja, R. a. Myllylä, J. M. Harja, J. Nikkinen, O. Tervonen, and V. Kiviniemi, "Fibre optic sensor for non-invasive monitoring of blood pressure during MRI scanning.," *Journal of biophotonics*, Vol. 4, no. 1-2, pp. 98–107, 2011.

114. Nakamura, T., Y. Inoue, D. Kim, N. Matsuhisa, T. Yokota, T. Sekitani, T. Someya, and M. Sekino, "Basic characteristics of implantable flexible pressure sensor for wireless readout using MRI," *Transactions of Japanese Society for Medical and Biological Engineering*, Vol. 52, pp. O–409–O–410, 2014.

115. Wentland, A. L., T. M. Grist, and O. Wieben, "Review of MRI-based measurements of pulse wave velocity: a biomarker of arterial stiffness.," *Cardiovascular diagnosis and therapy*, Vol. 4, no. 2, pp. 193–206, 2014.